UNITED NATIONS EDUCATIONAL, SCIENTIFIC AND CULTURAL ORGANIZATION
INTERNATIONAL CENTRE FOR THEORETICAL PHYSICS
I.C.T.P., P.O. BOX 586, 34100 TRIESTE, ITALY, CABLE: CENTRATOM TRIESTE

H4.SMR/650-13

Workshop on Three-Dimensional Modelling
of Seismic Waves Generation
Propagation and their Inversion

30 November - 11 December 1992

Characterization of Stong Ground Motion and Wave Propagation Based on Smart-1 Array

C. S. Oliveira

Ministerio das Obras Publicas
Laboratorio Nacional de Engenharia Civil
Lisbon
Portugal

CHARACTERIZATION OF STRONG GROUND MOTION AND WAVE PROPAGATION BASED ON SMART-1 ARRAY

by Carlos S. Oliveira

TOPICS TO BE COVERED

1- INTRODUCTION TO THE ENGINEERING SEISMOLOGY PROBLEM OF DEFINITION OF STRONG GROUND MOTION

2- PARAMETERS & VARIABLES NEEDED TO PERFORM ENGINEERING ANALYSIS OF A STRUCTURE

3- GROUND MOTION MAIN DESCRIPTION AND CHARACTERISTIC PARAMETERS

4- CONCEPT OF AN ARRAY

5- ARRAY TECHNIQUES FOR DATA TREATMENT

6- SMART-1 ARRAY. DESCRIPTION AND OBSERVATIONS

- WAVE IMAGE
- VARIABILITY OF STRONG MOTION PARAMETERS
- ROTATIONAL COMPONENTS
- POLARIZATION OF MOTION
- ATTENUATION OF STRONG GROUND MOTION
  INFLUENCE OF SOURCE AND SITE CONDITIONS
- F-K ANALYSIS
- COHERENCY STRUCTURE

7- FINAL CONSIDERATIONS

ICTP, 8-11/Dec/92

VARIABILITY OF STRONG GROUND MOTION. INFLUENCE OF LOCAL CONDITIONS AND INSTRUMENT ORIENTATION.

Fernando PIMENTEL [1], Carlos S. OLIVEIRA [2] and João AZEVEDO [3]

[1] Research Assistant, CMEST, Technical University of Lisbon *.
[2] Researcher , Laboratório Nacional de Engenharia Civil *.
[3] Associate Professor, CMEST, Technical University of Lisbon *.
* Lisbon, Portugal.

SUMMARY

The analysis of the variability of strong ground motion, namely the influence of the local conditions and instrument orientation, is made based on information available from the SMART-1 array in Taiwan. The study focuses on the distribution of the peak values and the variability of these peak values from site to site. It can be concluded that local variability of the earthquake motion is important enough not to be ignored in the forecasting of the severity of the strong ground motion. The same conclusions apply to the variability of the response spectra. Also studied is the influence of the instrument orientation showing that accurate information can only be obtained if the earthquake is looked at on its 3-dimensional content.

INTRODUCTION

This research work provides an useful insight on the study of the variability of strong ground motion from site to site. It was made with the records of 35 earthquake events occurred in Taiwan, obtained on the SMART-1 array (Ref.1).

In a previous work (Ref.2); variability of ordered peaks was studied. In here, a possible explanation of the causes of variability is presented, by looking simultaneously at the three-component acceleration vector and extending the analysis of variability to response spectra of the same records.

SMART-1 (**S**trong **M**otion **A**rray in **T**aiwan) is a dense seismic array located in the northeast corner of Taiwan near the city of Lotung. The array consists of a set of 36 force-balanced triaxial accelerometers displayed evenly in three concentric circular rings of radii 200, 1000 and 2000 m and one at the center as shown in Fig. 1. All stations are placed at the surface of a relatively flat recent alluvium made of a 15-20 m thick gravel topping a gray silt clay. Water table is almost at the surface.

Taiwan is part of a zone of high seismicity with a complex tectonic environment. This environment originates several types of source-mechanism earthquakes, which combined with different ranges of magnitude events and focal distances, suggests a classification of the events into 4 classes (Ref.2), as presented in Fig. 2:

1 - Nearby shallow small amplitude earthquakes, originated most probably at small size shallow faults (M_L in the range 3-4).
2 - Medium to large magnitude events (M_L in the range 5-8) occurring at great depths (50-100 Km), underneath the array, probably related to the dipping subduction.

3 - Shallow moderate to large magnitude events at intermediate distances from the array (15 to 30 Km). The tectonic mechanism should be similar to the one referred in 1.
4- Distant (larger than 50 Km) moderate to large magnitude events at moderate depths.

Fig. 2 is a global representation of the hypocentral distance with respect to the array and irrespectively of the azimuth. For each class a typical event was chosen and its location signaled (* 35, 30, 32 and 24).

The 35 events were recorded in the array between September 1980 and September 1985, and were classified according to the previous criteria. These events which produced strong motion at 712 different situations, were recorded in 3 orthogonal components: NS, EW and vertical (DN).

STATISTICAL DISTRIBUTION OF THE ORDERED PEAKS

Assume that a peak is the largest value of a set of recorded accelerations with the same sign. The peaks are ordered by decreasing absolute value and the first one is the peak ground acceleration, PGA (x1).

Usually the distributions of the ordered peaks are studied by either the Exponential, Rayleigh or Weibull laws (Ref.3). Fig. 3 presents the general trend of these three distributions plotted on exponential probability paper. Rayleigh distributed peaks are concentrated in the high acceleration part, whereas in the Weibull distribution they concentrate in the lower acceleration zone.

In this study the type of distribution that better characterizes the data set is analyzed. The selection criteria is based on minimization of the mean square error (Ref.4). Fig. 4 presents the relative percentage of the different types of distributions for each class. Fig. 4a refers to horizontal components and Fig. 4b to the vertical component. As it can be observed from these figures, there is a large tendency for Exponential and Rayleigh distributions. Weibull type is only observed for horizontal components and classes 1 and 3 (short hypocentral distances). The tendency for Rayleigh distributed ordered peaks is largely noted for class 4 events (large epicentral distances)

VARIABILITY OF FIRST ORDERED PEAKS FROM SITE TO SITE

The repetition of this analysis for other stations showed great variations not only in the PGA values for each station but also in the type of distribution. Fig. 5 shows the qualitative variation of PGA throughout the array for event 32, components NS and vertical. The extension of this study to the 35 events showed that there is no common trend on this variability: no relation to the type of earthquake mechanism or class and no relation to geology.

The variations in PGA for a given event, measured as a ratio of high to low value, varies from 2:1 to a maximum of 6:1. The coefficient of variation $\sigma/\bar{x}$ varies from a minimum of 0.17 to a maximum of 0.49. The largest variations are observed in nearby earthquakes. Fig. 6 presents the statistical distributions of PGA values recorded in all stations for 4 different events, one in each class, emphasizing the dependence on class and component. The variability is not, however, very much dependent on distance among stations, as can be seen in Fig. 7, where the ratio of PGA (event *24-NS) for any possible combination of two stations is plotted against distance between them.

The study of the 2nd, 3rd,... 11th peak values across the array was also made. Fig. 8 shows, for each class of events, the average decrease of the mean values of these

ordered peaks with respect to the order number. The decrease is rather smooth following approximately an exponential type law. Differences among classes reflect the predominance of the distributions referred in the previous section. The coefficients of variation are almost independent of the order number and depend also on class and component. Values vary between 0.15 to 0.3 for horizontal components and between 0.25 to 0.4 for vertical components.

INFLUENCE OF INSTRUMENT ORIENTATION

How does instrument orientation influence previous findings ?

In reality ground motion is a 3 component entity which is not invariant under a change of the reference system. Several authors have addressed this problem (Ref.5) trying to identify principal directions of motion, and correlating them to the epicentral orientation. Imagine an horizontal rotation of a station by an angle α . The distribution of the ordered peaks of the record obtained in that station, was studied and is presented in Fig. 9. Each curve corresponds to a given order peak. On the lower portion of Fig. 9 the type of distribution which better fits the data is plotted against the angle α . Several comments should be made:

a) There is a remarkable dependence of both, the peak values (PGA included) and types of distribution on the orientation of the instrument.

b) PGA values vary 1: 1.8 as shown in the figure.

c) The higher and lower PGA values occur at approximately 90º apart denoting the presence of principal directions as obtained for the first three peaks (1st, 2nd and 3rd) for the different stations during event #24. Fig. 10 shows that there is some consistency among all stations.

d) An analysis of the peak values in just any two orthogonal directions without taking into consideration the above mentioned features, may lead to quite erroneous estimates. In the present case to a value which is approximately 75% of the maximum possible (see Fig. 9 at α = 115º and α = 205º).

e) The type of distribution is very much dependent on the larger values, near the principal direction.

In the previous analysis the records were looked at in their globality, loosing their time evolution. If the time evolution of the horizontal acceleration values (as a function of its amplitude and direction is analysed, the "record" has an aspect as shown in Fig. 11, which consists on a dimetric projection of the acceleration vector as a function of time (event #24, station 103). It is clear from this figure that there are sudden changes both in the amplitude and direction of the motion indicating that there should be a definition for peak value which could consider this aspect.

In Fig. 12 the NS and EW components and the absolute horizontal value of the acceleration vector (event #24, station 101) are presented, showing that it is necessary to deal with both components (time envelope of the record) if a more realistic analysis of the peak values is to be made.

RESPONSE SPECTRUM ANALYSIS

The influence of the class of the earthquake on the average 5% damping response spectra is represented in Fig. 13. The average is made for all the EW records in all the stations and for all the earthquakes belonging to a given class, normalized to the same PGA value (0.175 g). It is remarkable the difference between the spectra, especially for classes 1 and 4. For each class the variability of the spectra (not shown) is of the same order of the variability of the peak values.

ACKNOWLEDGMENTS

Data from SMART-1 records were kindly provided by the Seismographic Station, University of Califórnia, Berkeley.

REFERENCES

1 - Bolt, B. A. ; Loh, C. H. ; Penzien, J. ; Tsai, Y. B. and Yeh, Y. T. (1982) " Preliminary Report on SMART-1 Strong Motion Array in Taiwan", Report UCB/EERC-82/13, University of California, Berkeley.

2 - Oliveira, C. S. ; Pimentel, F. and Azevedo, J. (1986) " Variability of Strong Ground Motion Ordered Peaks at a Site, Based on Dense Seismic Array", Proc. 8th European Conf. Earthq. Eng., Vol. 6, LNEC, Lisbon.

3- Azevedo, J. (1984) " Characterization of Structural Response to Earthquake Motion", Ph. D. Dissertation, Dep. Civil Eng., Stanford Univ., Stanford.

4- Pimentel, F. (1987) " Análise da Variabilidade da Acção Sísmica " M.Sc. Thesis, Technical University of Lisbon, Lisbon (In Portuguese).

5- Penzien, J. and Watabe, M. (1975) "Characteristics of 3-Dimensional Earthquake Ground Motions" Journal of Earthq. Eng. & Struct. Dyn., Vol 3, pp 365-373.

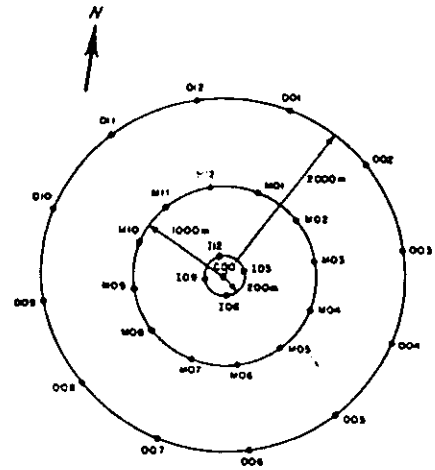

Fig. 1 - Stations location in Array Smart-1.

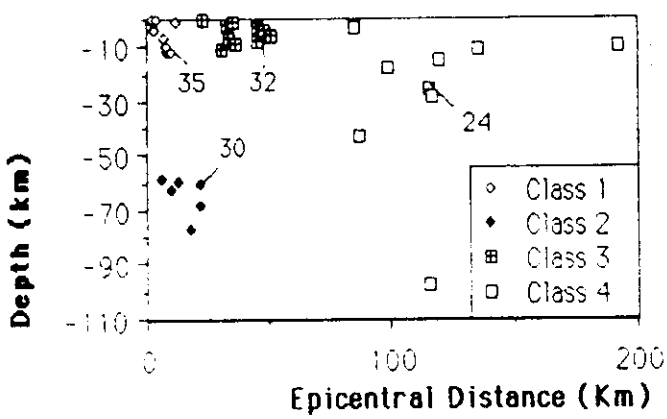

Fig. 2 - Hypocentral location of the recorded events.

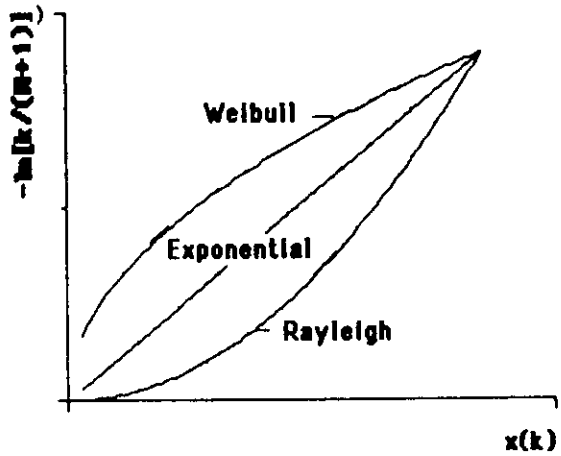

Fig. 3 - Ordered peak distributions.

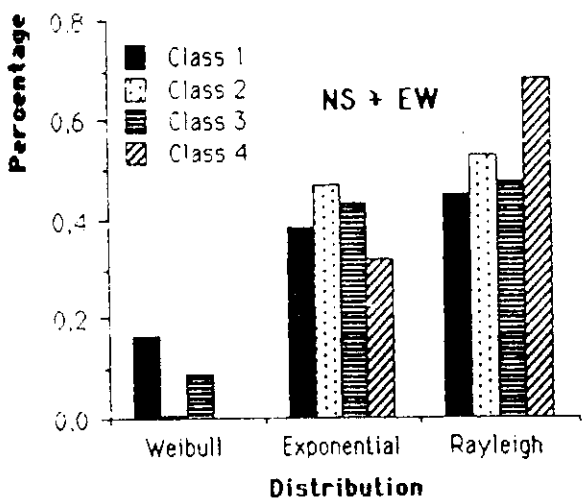

a) NS + EW Components

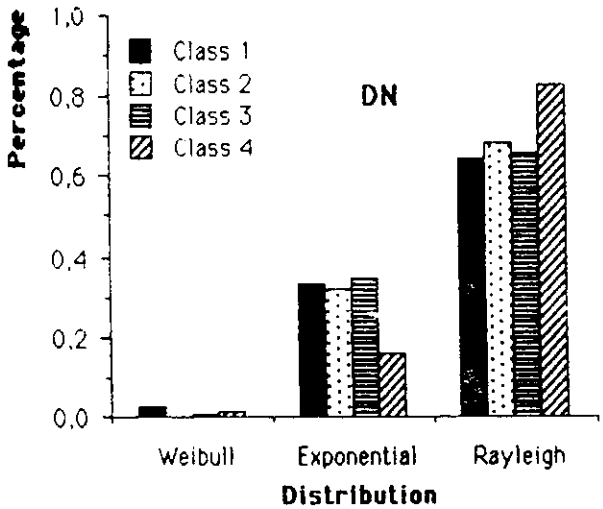

b) DN Component

Fig. 4 - Relative percentage of type of distributions for each class of events.

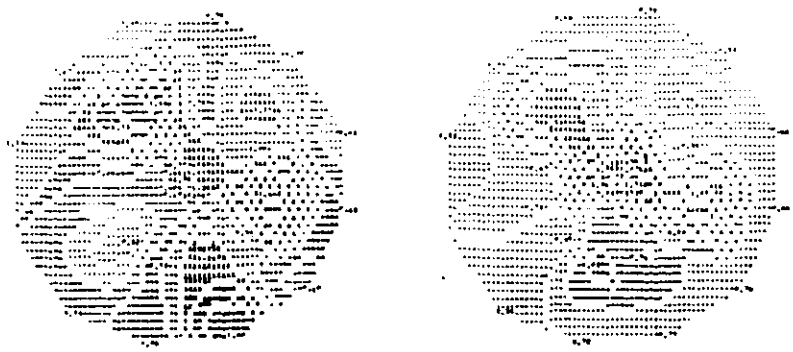

a) EVENT 32 - NS Component b) EVENT 32 - DN Component

Fig. 5 - Variability of 1st peak across the array.

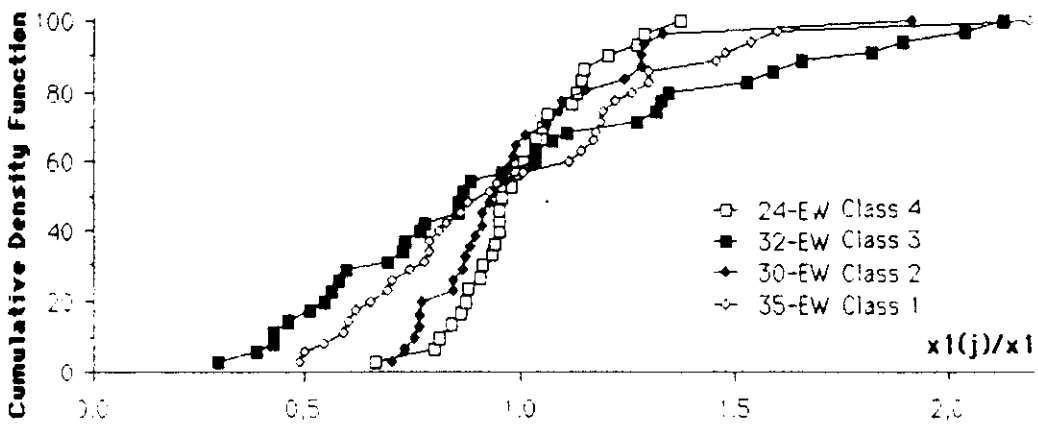

Fig. 6 - Statistical distributions of the PGA values across the array.

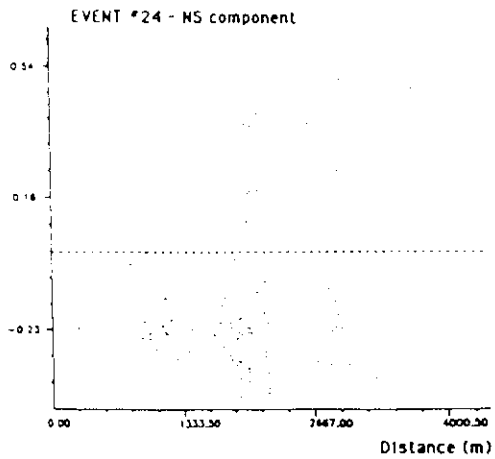

Fig. 7 - Interstation variability of PGA values.

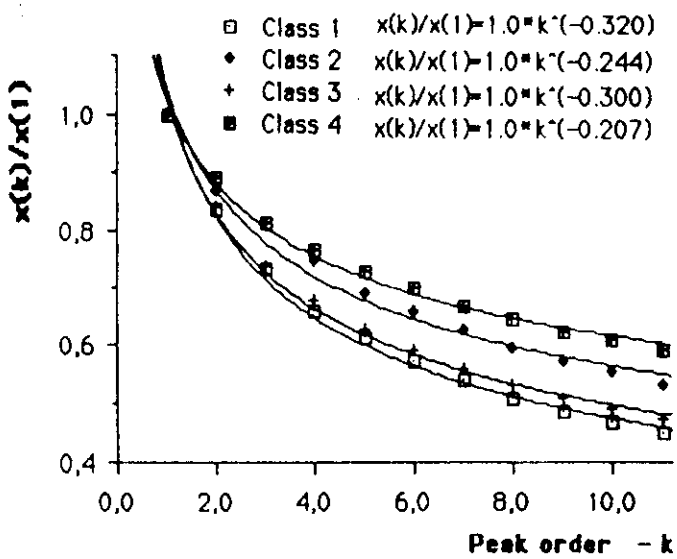

Fig. 8 - Decrease of peak value with the peak order.
(Average for all stations)

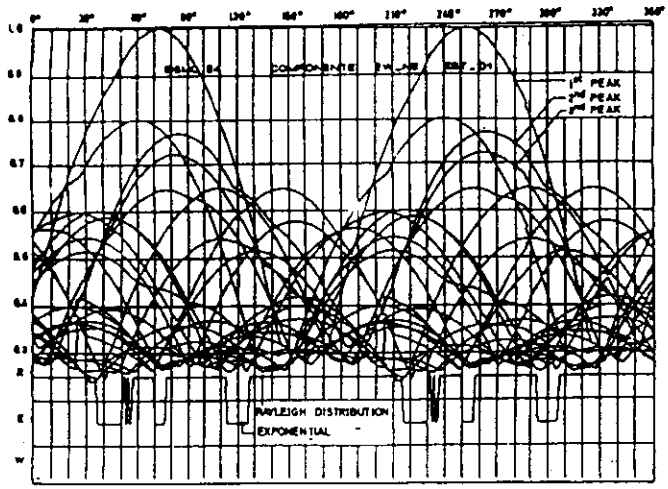

Fig. 9 - Influence of the station orientation in the peak values.

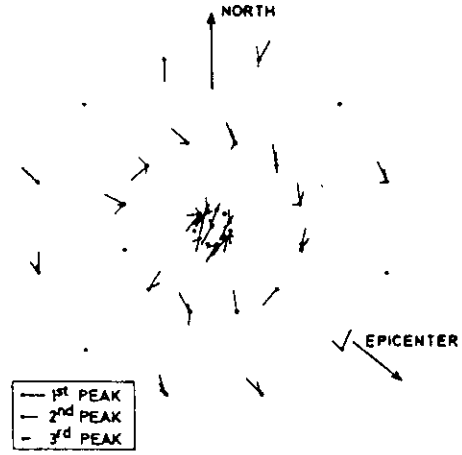

Fig. 10 - Orientation of the 3 largest peaks across the array (Event 24).

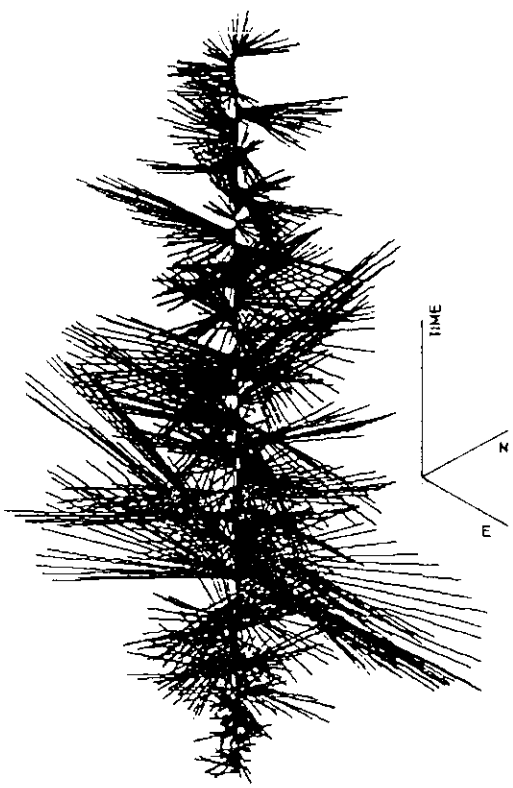

Fig. 11 - Dimetric projection of the time evolution of the acceleration vector.

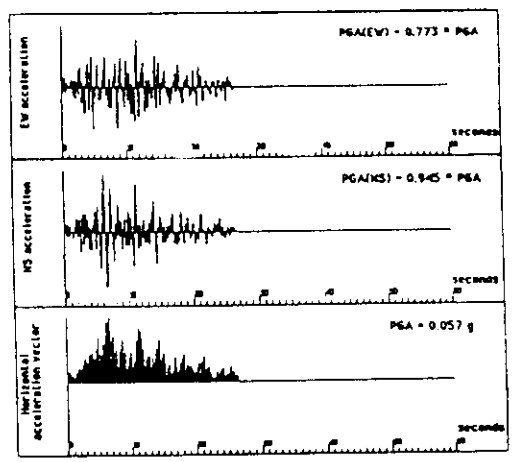

Fig. 12 - Influence of station orientation on the record. Event 24 - (NS, EW component - Vector amplitude)

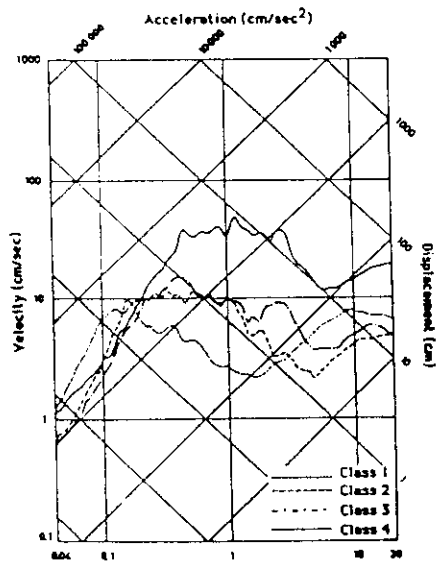

Fig. 13 - Mean value response spectra.

A-10

EARTHQUAKE ENGINEERING AND STRUCTURAL DYNAMICS, VOL. 18, 517–526 (1989)

ROTATIONAL COMPONENTS OF SURFACE STRONG GROUND MOTION

CARLOS S. OLIVEIRA

Laboratorio Nacional de Engenharia Civil, Avenida do Brasil, 1799 Lisbon, Portugal

AND

BRUCE A. BOLT

Seismographic Station, University of California, Berkeley, California 94720, U.S.A.

SUMMARY

Rotational components of seismic waves have been estimated using the strong motion array in Taiwan, SMART-1. The inner rings of accelerographs, covering an approximately circular area of 3 km^2, permit a decomposition of travelling waves with wavelengths in the range 0·5 to 5·0 km and frequencies from 0·1 to 5 Hz.

Rotational components of the strain field, obtained from station pairs and averaged over the array using stacking techniques, were computed for five different earthquakes with M_s magnitude 5·7 to 7·8, and epicentral distances 6 to 84 km. The results indicate peak rotation values about a vertical axis on the order of 4×10^{-5} rad at an approximately 2·5 s period. The measured values for pure rotation and rocking are in agreement with the spatial coherency structure observed in these earthquakes. For comparison, significant effects to engineered structures generally appear when curl $\theta > 10^{-4}$ rad. The estimates are important for design of scaled engineered models for soil–structure interaction experiments.

INTRODUCTION

Rotational components of strong seismic ground motion have been discussed in the literature for many years. Richter[1] attributed to rotational wave components the rotational offsets observed after earthquakes in massive rocks, tombstones and in the upper part of chimneys. Nevertheless, despite numerous ingenious attempts, until the present it has not been possible to measure directly the rotational components of ground motion even though the basic response of some seismological instruments such as the Wood–Anderson seismograph and early model accelerometers relies on the relative rotation of a torsional pendulum but do not provide ground rotation directly. Perhaps the first published material on measured torsional components in strong ground motion was made by Shibata *et al.*[2] Their results obtained through a moving coil-type torsional motion pick-up contain, however, coupling with horizontal motion.

Newmark[3] emphasized that the rotational components of ground motion could be of importance in the design of engineered structures. His argument was based on the concept of a monochromatic plane wave travelling with an apparent velocity similar to that of a shear wave in the surface rock or soil layer. For soft soil conditions, with shear velocities in the range of 100 to 300 m/s, this model leads to rotations on the order of 10^{-3} rad, inducing significant stresses in certain types of structures. With a similar approach, Stratta and Griswold[4] used the displacement in monochromatic wave propagation to produce a relative rotation between adjacent columns supporting a rigid slab, and they demonstrated that structural collapse might occur when rocking was of the order of 50×10^{-4} rad. Since then, further concern has been expressed in earthquake engineering regarding effects of the rotational components of ground motion, with the result that at least one building code, ATC 3-06, now contains extensive material on practices that, implicitly or explicitly, take rotational motion into consideration.

0098–8847/89/040517–10$05.00

Received 2 June 1988
Revised 19 October 1988

From the theory of elastic waves, the shear S, Love and Rayleigh waves all involve rotational strain while the compressional P waves do not. Let **u** be the ground displacement at a point due to seismic motion. The relative importance of each of the three components of curl **u** depends on the type of structure under consideration. For tall structures, both rocking and torsion become important,[5] whereas for small and rigid structures only rocking may be important.

Recently, algorithms allowing inclusion of torsional motions in engineering application have been developed along two main lines: (i) analytical studies based on physical models of the source and propagation; and (ii) methods for generating both response spectra and compatible time-series.

Work using physical modelling has been done by Bouchon and Aki[6] in relation to the Imperial Valley fault which produced the 1979 earthquake. They simulated mathematically a strike-slip fault undergoing a total relative displacement of 1 m (approximately equivalent to a magnitude $M_L = 6{\cdot}5$ earthquake), and computed the strain field for different locations (Figure 1). Torsion and rocking components of ground motion obtained along a transverse profile to the fault trace (Figure 1) show that the peak rotations decrease quite rapidly with distance to the fault. Observationally at 5 km from the fault, the instrumental measurements yielded peak values on the order of 10^{-4} rad. They also found that the attenuation depends on the type of wave present and on lateral crustal heterogeneities. Simplified models of monochromatic waves were found to produce satisfactory fits only if the apparent velocity is the shear velocity in the basement rock or the rupture velocity on the fault. This result throws into doubt the initial assumption of Newmark, that the appropriate apparent velocities were much smaller.

On the engineering side, based on refraction of seismic waves at the ground surface, Trifunac[7] derived the response spectrum for the rotational components of seismic ground motion from a harmonic translational component at the surface. Subsequently, Lee and Trifunac[8] developed torsional accelerograms compatible with an artificial translational accelerogram with a given proportion of surface and body waves. Other researchers[9-12] used similar techniques to compute rotational response spectrum. Several studies,[13,14] made in recent years, were concerned with the response of engineered structures to horizontally propagating waves but did not include the rotation feature.

None of the above studies, however, have had the benefit of testing against field measurements. The first values of ground rocking measured with some precision were obtained by Niazi[15] from analysis of the three components of recorded acceleration along the El Centro linear differential array during the 1979 Imperial Valley earthquake. This array, located approximately 5 km from the fault trace, consists of 5 aligned recording stations 18 m apart sub-parallel to the fault. Niazi computed peak rotational values of 50×10^{-4} rad when only adjacent stations were used; these values dropped to 10^{-4} when larger station separations were considered. Table I summarizes the results obtained in past studies of the 1979 Imperial Valley earthquake.

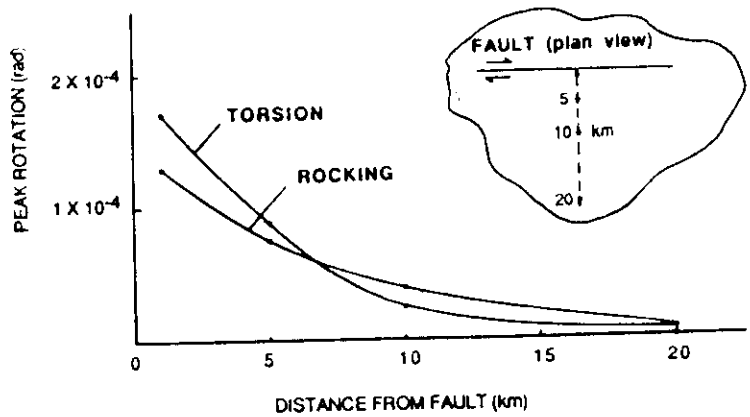

Figure 1. Peak rotation values obtained by analytical simulation, along a profile perpendicular to a strike-slip fault that undergoes 1 m displacement (adapted from Bouchon and Aki[6])

Table I. Past studies of rotational components (1979 Imperial Valley earthquake)

Author	Type of study	Peak rotation
Niazi[15]	Measurements El Centro differential array	10^{-3} rad ($d = 18$ m)
	Fault at < 5 km	2×10^{-4} rad ($d > 18$ m)
Bouchon & Aki[6]	Analytical simulation Fault at < 5 km	7×10^{-5} rad

OBSERVATIONAL BASIS AND ANALYSIS

Circular arrays of seismic sensors, with adequate timing, can measure curl **u** directly. In an attempt to explore the experimental uncertainties, we have used data from five earthquakes recorded at the strong motion array in Taiwan, SMART-1. The array consists of 37 triaxial three-component force-balanced accelerometers arranged in three concentric circular rings of radii 200, 1000 and 2000 m, and one at the centre (Figure 2). The rings with 12 equally spaced stations are named I(inner), M(middle) and O(outer), respectively; the centre station is C-00. The distances between station pairs vary from a minimum of approximately 105 m to a maximum of 4000 m.

The five earthquakes studied are listed in Table II with numerical designations 5, 24, 39, 43 and 45. They are among the largest events recorded by the array and cover a range of magnitudes and epicentral distances

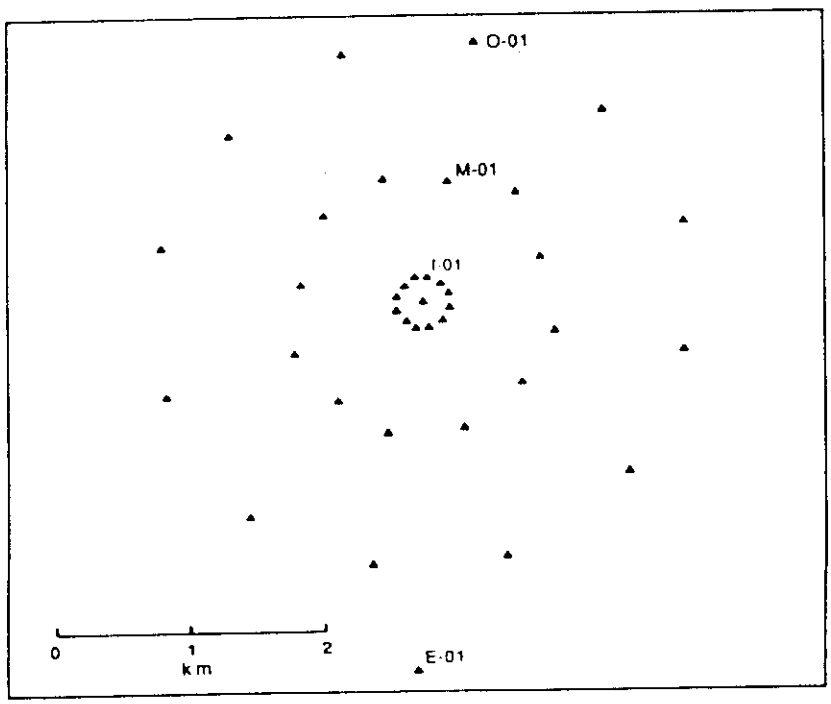

Figure 2. SMART-1 array configuration and reference system

Table II. Characteristics of SMART-1 earthquakes

Event	Origin time	Mag. (M_s)	Dist. (km)	Azimuth (N–E)	Depth (km)	PGA (max) (cm/s^2)	PGD (max) (cm)
# 5	1981.01.29 04:51:34·5	5·7	30	149°	25	Horiz.—244 Vert. — 64	Horiz.— 2·5 Vert. — 0·5
# 24	1983.06.24 09:06:46·3	6·7	84	124°	48	Horiz.— 65 Vert. — 15	Horiz.— 2·0 Vert. — 0·5
# 39	1986.01.16 13:04:32·0	5·8	22	64°	10	Horiz.—375 Vert. —314	Horiz.—10·0 Vert. — 0·6
# 43	1986.07.30 11:31:47·5	5·6	6	150°	2	Horiz.—283 Vert. —224	Horiz.— 6·0 Vert. — 0·6
# 45	1986.11.14 21:20:01·2	7·8	79	175°	7	Horiz.—238 Vert. —104	Horiz.— 8·5 Vert. — 2·5

(Figure 3). Event 45 is the largest earthquake to trigger the SMART-1 array since its installation in 1980 and the seismic ground motion caused considerable damage in north Taiwan. All events show highly spatially correlated ground motion during the arrival of the S waves and sometimes in the coda. This is more clear in the displacement traces (Figure 4), and especially for those events, with larger magnitude and larger epicentral distance, which have a consistently lower frequency content throughout the total duration of

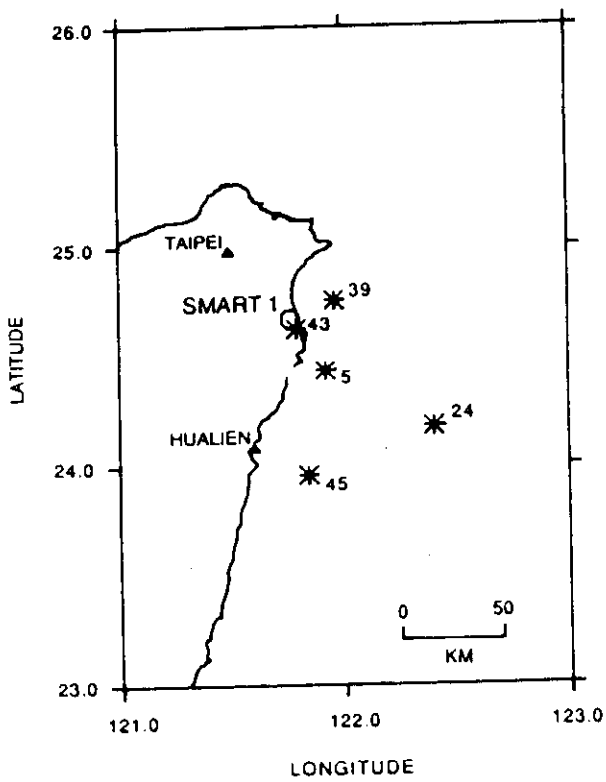

Figure 3. Epicentral locations of events under study (latitude and longitude in degrees)

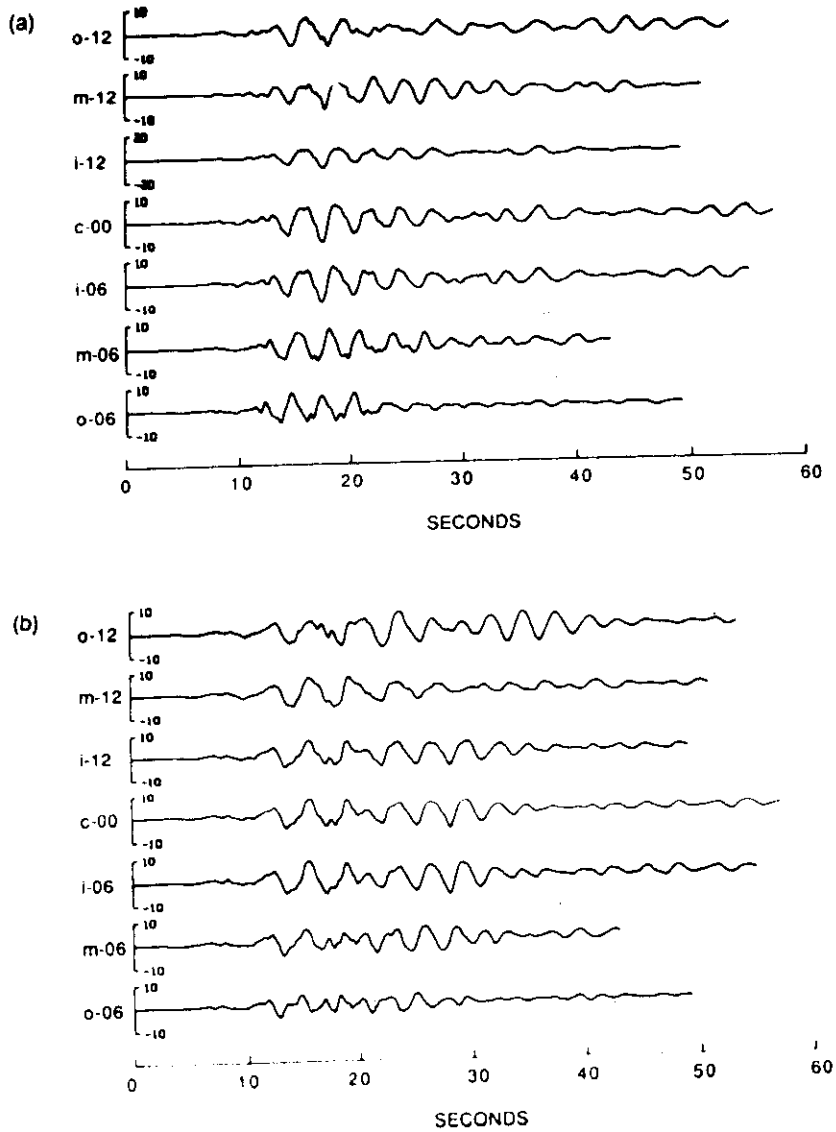

Figure 4. Displacement traces (in cm) of horizontal components for event 45 across the array: (a) North–South component; (b) East–West component

motion. Maximum ground wave displacements range between 2 and 10 cm at SMART 1. More detailed information on these events is published.[16, 17]

Corrected accelerograms were computed using a low frequency cutoff at 0·1 Hz and a high cutoff at 25·0 Hz, and subsequently velocities and displacements were computed. The integrations were made in the frequency domain. Direct and inverse FFT algorithms were used, after removal of a constant term, together with a bandpass 6-pole Butterworth filter applied in the direct and reverse time axis to remove phase distortions. Comparisons between the 6-pole and the Ormsby filter as used in standard USGS procedures were made, and the results were similar. The influence of filter parameter values on displacements was checked, and for frequencies above 0·15 Hz, the results comparing particle motions at adjacent stations were not sensitive to these variables.

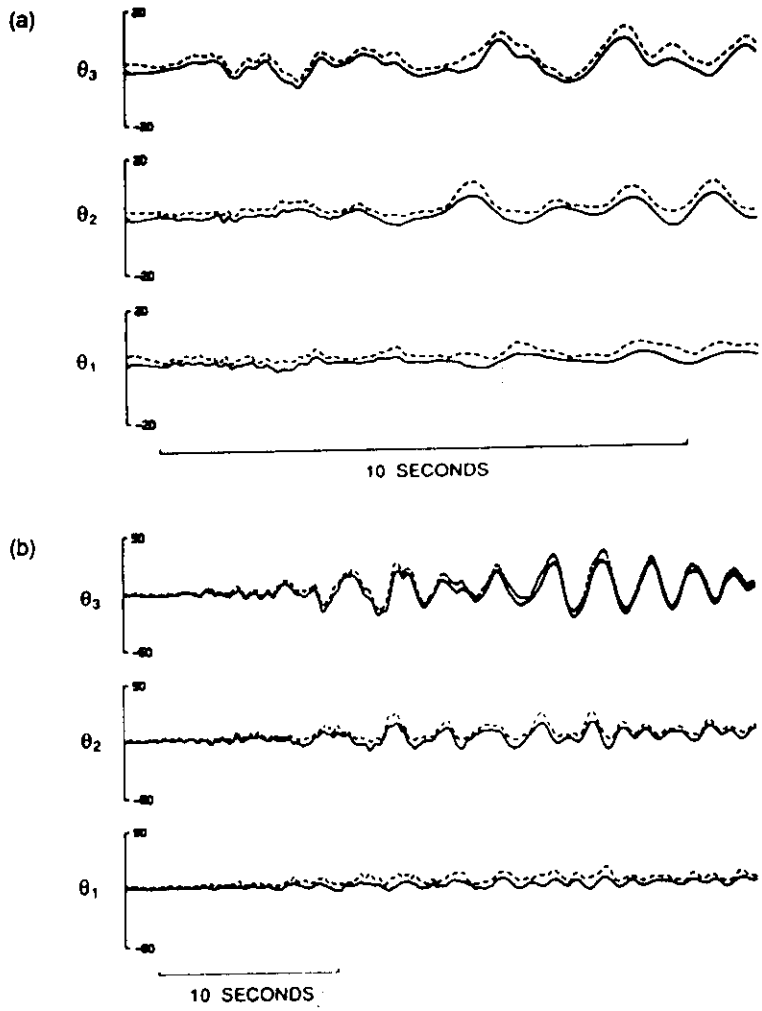

Figure 5. Three component rotational time-histories ($\times 10^{-6}$ rad) computed for inner-ring stations: (a) event 43; (b) event 45. Continuous lines denote mean values and dashed lines denote mean plus one standard deviation

larger station separation increases the scatter significantly so that ground rotation is no longer resolved with the simple stacking technique used. The introduction of time lags selected to yield maximum correlation before stacking slightly improves the rotational estimates, but the results become highly dependent on the selected time window.

(vi) Filtering, using the two frequency windows referred to above, shows that the main energy contributing to the larger rotational components is contained in the range 0·2 to 1·0 Hz. In the range 1·0 to 5·0 Hz, rotations are still present but with smaller amplitudes; above 5·0 Hz, rotational components cannot be detected by SMART 1 in these earthquakes. The result is no doubt related to the lack of spatial coherency of wave components at the high frequencies[18] and perhaps errors in spatial coordinates of each station.

(vii) Results obtained starting either from displacements or accelerations are approximately the same, with variations on the two extremes of the spectral content. Differentiation introduces spurious high frequency glitches and integration introduces long period oscillations. In both cases adequate filtering reduces the problem.

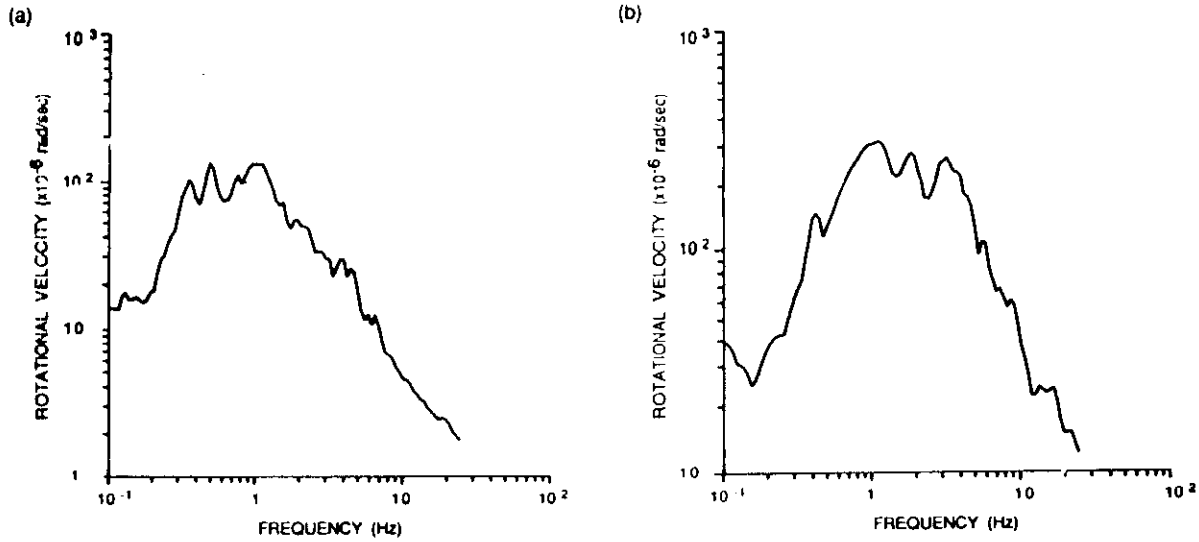

Figure 6. Pseudo angular velocity response spectrum of θ_3 component for: (a) event 24; (b) event 39 (damping ratio $\xi = 0{\cdot}05$)

Table III. Rotation peak values

Event	Comp.	θ ($\times 10^{-6}$ rad)	$\ddot{\theta}$ ($\times 10^{-6}$ rad/s^2)
5	torsion	8·5	940
	rocking	4·4	512
24	torsion	6·8	270
	rocking	5·7	83
39	torsion	14·6	1324
	rocking	5·1	2458
43	torsion	7·4	
	rocking	5·7	
45	torsion	39·3	915
	rocking	12·8	

Figure 7 correlates the relevant mean peak acceleration values observed for each event with the mean peak torsional and rocking components. In the case of rocking there is a systematic trend, but this correlation is not clear with the torsional component, a result perhaps explained by the low frequency content of the ground displacement.

CONCLUSIONS

The stacking technique used for estimating the rotational components of ground motion was found to be effective for array analysis. The SMART 1 array is not able to detect rotational components for frequencies above 5·0 Hz, but at lower frequencies the maximum measured average result of 4×10^{-5} rad (with a 0·15 coefficient of variation) is consistent with previous estimates of Niazi[15] and Bouchon and Aki[6] on the assumption that the wave attenuation over the epicentral distances used here is relatively large. It should be

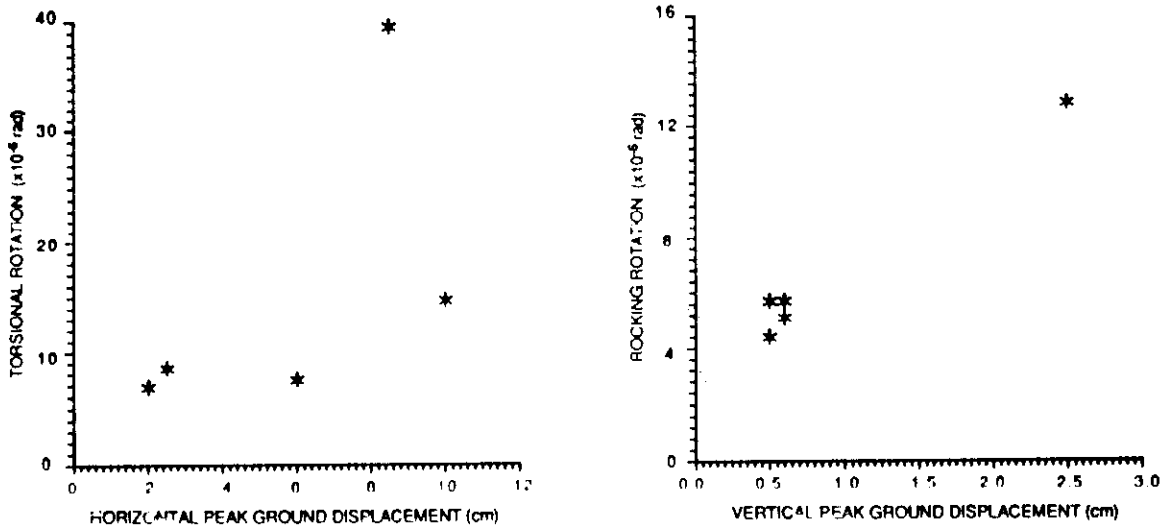

Figure 7. Peak ground rotation as a function of peak ground displacement

bourne in mind, however, that the SMART 1 array is located at Lotung in a water-saturated alluvial basin which may induce some site specific rotational behaviour.

With the caution given above, the observed values from the moderate earthquakes discussed here suggest that, for epicentral distances greater than 30 km and magnitudes smaller than 7, the pure free-field rotational components of ground motion would contribute little to the response of engineered structures (in the frequency range 0·2 to 5 Hz). Nevertheless, for sites nearer the seismic source, rotations may be important, as indicated by the measurements in the 1979 Imperial Valley earthquake.

Additional measurements of pure rotation and rocking components of seismic wave motion are much needed for structural considerations.[10-12] Answers to questions on the structural response of high rise buildings and other major and critical buildings to torsional seismic wave components require a much greater data base than is now available.

ACKNOWLEDGEMENTS

This study was conducted during the leave of the first author, from the Laboratorio Nacional de Engenharia Civil, Lisboa, at the Seismographic Station, University of California, Berkeley, and was supported by National Science Foundation under Grant No. ECE 8417856.

REFERENCES

1. C. F. Richter, *Elementary Seismology*, W. H. Freeman, San Francisco, 1958.
2. H. Shibata, T. Shigeta and A. Sone, 'On some results of observation of torsional ground motions and their response analysis', *Bull. ERS* **10**, 43–47 (1976).
3. N. M. Newmark, 'Torsion in symmetrical buildings', *Proc. 4th world conf. earthquake eng.* Santiago do Chile, **II**, A3.19–A3.32 (1969).
4. J. L. Stratta and T. F. Griswold, 'Rotation of footing due to surface waves', *Bull seism. soc. Am.* **66**, 105–108 (1976).
5. G. C. Hart, M. DiJulio and M. Lew, 'Torsional response of high rise buildings', *J. struct. div. ASCE* **101**, 397–414 (1975).
6. M. Bouchon and K. Aki, 'Strain, tilt, and rotation associated with strong ground motion in the vicinity of earthquake faults', *Bull. seism. soc. Am.* **72**, 1717–1738 (1982).
7. M. D. Trifunac, 'A note on rotational components of earthquake motions on ground surface for incident body waves', *Soil dyn. earthquake eng.* **1**, 11–19 (1982).
8. V. M. Lee and M. D. Trifunac, 'Torsional accelerograms', *Soil dyn. earthquake eng.* **4**, 132–139 (1985).
9. N. D. Nathan and J. R. MacKenzie, 'Rotational components of earthquake motion', *Can. j. civil eng.* **2**, 430–436 (1975).
10. A. Rutenberg and A. C. Heidebrecht, 'Response spectra for torsion, rocking and rigid foundations', *Earthquake eng. struct. dyn.* **13**, 543–557 (1985).
11. W. K. Tso and T. I. Hsu, 'Torsional spectrum for earthquake motions', *Earthquake eng. struct. dyn.* **6**, 375–392 (1978).

12. A. Castellani and G. Boffi, 'Rotational components of the surface ground motion during an earthquake', *Earthquake eng. struct. dyn.* **14**, 751–767 (1986).
13. J. P. Wolf, P. Obernhuber and B. Weber, 'Response of a nuclear power plant on aseismic bearings to horizontally propagating waves', *Earthquake eng. struct. dyn.* **11**, 483–499 (1983).
14. J. E. Luco, 'Response of a rigid foundation to a spatially random ground motion', *Earthquake eng. struct. dyn.* **14**, 891–908 (1986).
15. M. Niazi, 'Inferred displacements, velocities and rotations of a long rigid foundation located at El-Centro differential array site during the 1979 Imperial Valley, California, earthquake', *Earthquake eng. struct. dyn.* **14**, 531–542 (1987).
16. C. S. Oliveira, 'Variability of strong ground motion characteristics obtained in SMART-1 array', *12th reg. seminar earthquake eng.* Halkidiki, Greece (1985).
17. R. B. Darragh, 'Analysis of the near-source waves: Separation of wave types using strong motion array recordings', *Ph.D. Thesis* University of California, Berkeley, CA. 1987.
18. N. A. Abrahamson and B. A. Bolt, 'Array analysis and synthesis mapping of strong seismic motion', in *Strong Motion Synthetics* (Ed. B. A. Bolt), Academic Press, Orlando, 1987.

Nuclear Engineering and Design 111 (1989) 293–310
North-Holland, Amsterdam

MULTIPLE-STATION GROUND MOTION PROCESSING AND SIMULATION BASED ON SMART-1 ARRAY DATA

H. HAO [1], C.S. OLIVEIRA [2] and J. PENZIEN [3]

[1] *University of California, Berkeley, USA*
[2] *Laboratório Nacional de Engenharia Civil, Av. Brasil, 1799, Lisboa, Portugal*
[3] *University of California, Berkeley, USA and Eastern International Engineers, Inc., Lafayette, California, USA*

Received 21 March 1988

This paper presents a method of generating multiple-support inputs for any given set of n surface locations having space coordinates x_i and y_i ($i = 1, 2, \ldots, n$) which are compatible with the main wave propagation properties observed in the Strong Motion Array Taiwan (SMART-1). Based on data collected in this array during two different earthquakes, a coherency function $\gamma_{ij}(d_{ij}^{L}, d_{ij}^{T}, f)$ is developed for pairs of stations, i and j, as a continuous function of frequency f and projected separation distances d_{ij}^{L} and d_{ij}^{T} in the longitudinal direction of preferential wave propagation and in the transverse direction, respectively. Using three different time windows, changes in apparent wave velocity and power spectral density are determined as functions of frequency by averaging such functions over the entire array. Finally, an average shape function for the entire time-history is obtained. This entire process was repeated for each of the three components of motion. Coherency between EW and NS components at each station was also investigated. The results presented herein are essentially valid for station separations up to 400m. An algorithm and procedures for generating spatially correlated ground motions which incorporate all of the above mentioned features are presented.

1. Introduction

For some time [1], consideration has been given to wave propagation as it affects the response of structures to strong ground motions. It has been recognized that spatial variations induce rotational components at individual sites and cause differential movements along the foundations of extended structures. Until recently, all such considerations have been based primarily on theoretical developments and on observations of overall structural behavior during earthquakes [2–4]. The study of strong ground motion characteristics acquired a new dimension, however, when high density arrays of accelerometers were developed. These arrays permit for the first time, among other features, the determination of spatial correlation of ground accelerations and displacements, the evaluation of variability of motion within a small area, the computation of ground strains, and the determinations of torsional and rotational components of ground motion. These characteristics are of importance in the definition of ground motions to be used for inputs into engineered structures, especially extended structures such as buried pipelines, tunnels, bridges, and dams. They are also of importance in defining the inputs to tall structures such as high rise buildings, towers, and chimneys, and the large rigid continuous foundations such as those of nuclear power plants.

In the present paper, selection and quantification of the main parameters controlling wave propagation are of primary concern. Using modern techniques for wave propagation detection and the SMART-1 (Strong Motion Array Taiwan) data recorded during two earthquakes, a methodology is developed for generating time series which are compatible with the correlation properties observed in the data. Such time series can be used as the design multiple input to important structures.

1.1. Description of SMART-1 array and its geological setting

The SMART-1 array with its 37 stations covering an approximate area of 12 km^2 is located in the northeast

[1] Graduate Student.
[2] Researcher.
[3] Professor Emeritus of University of California and Board Chairman of Eastern International Engineers, Inc.

0029-5493/89/$03.50

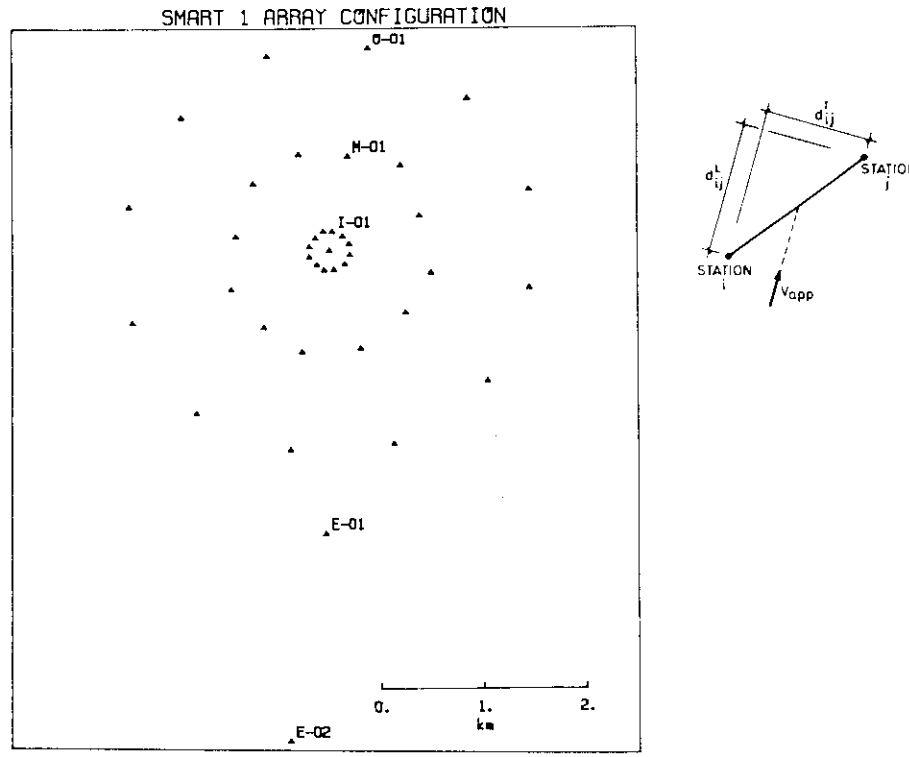

Fig. 1. Array configuration and location of recording stations.

corner of Taiwan near the city of Lotung. Its installation began in September 1980 and was completed by August 1982. By December 1987, 51 earthquake events had been recorded in this array, producing records with peak ground accelerations, PGA, ranging from 10 to 350 cm/s^2. About 3500 records are now available. The array consists of 12 triaxial strong-motion accelerometers located in each of three concentric circular rings having radii of 200 m, 1000 m, and 2000 m, and of one triaxial accelerometer located at the center of the array, fig. 1. The three rings with 12 equally spaced stations, numbered 1 through 12 clockwise are named I(inner), M(middle) and O(outer), respectively; the center station is named C-00. The distances between station pairs vary from a minimum of approximately 105 m to a maximum of 4000 m. In June 1983, stations E-01 and E-02, located respectively at 2.8 km and 4.8 km south of C-00, were added to the array. These latter two stations are installed on rock while all others are placed at the surface of a relatively flat alluvium having elevations ranging from 2.4 m to 18.1 m over the array. For a more complete description of the SMART-1 site conditions,

Table 1
Main characteristics of SMART-1 events under study

Event	Origin time	Mag (M_L)	Dist. (km)	Azimuth (N–E)	Depth (km)	PGA(max) (cm/s^2)	PGD(max) (cm)
#24	1983.06.24 09:06:46.3	6.7	84	124°	48	Horiz- 65 Vert- 15	Horiz- 2.0 Vert- 0.5
#45	1986.11.14 21:10:01.2	7.8	79	175°	7	Horiz-238 Vert- 104	Horiz- 8.5 Vert- 2.5

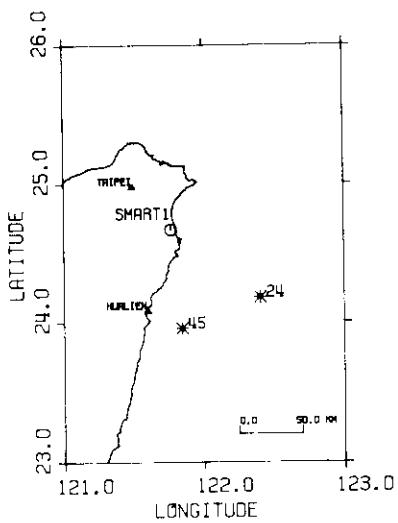

Fig. 2. Epicentral location of events under study.

and its station coordinates and instrumentation, see Bolt et al. [5] and Abrahamson [6].

1.2. Summary of main properties of the recorded earthquakes

To study wave propagation in the SMART-1 basin and to characterize the main properties associated with it, two earthquakes listed in table 1 as events numbers 24 and 45 were selected. As indicated, these events had magnitudes of 6.7 and 7.8, epicentral distances of 84 and 79 km, fig. 2, peak ground accelerations (PGA) of 65 and 238 cm/s^2, and peak ground displacements (PGD) of 2.0 and 8.5 cm. Event No. 45, the largest earthquake to trigger the SMART-1 array since its installation in 1980, caused considerable damage in north Taiwan. The events referenced in table 1 produced highly spatially correlated ground motion during the arrival of the S waves [7]. Fig. 3 presents the N–S components of acceleration recorded during events numbers 24 and 45 (For more detailed information on these events see Oliveira [7], Darragh [8], and Bolt and Chiou [9].)

2. Theoretical considerations on wave propagation and multi-signal processing

2.1 Basic theory

The general representation of ground motion at any station location $P(x, y, z)$, consists of time and/or frequency domain descriptions of the three translational

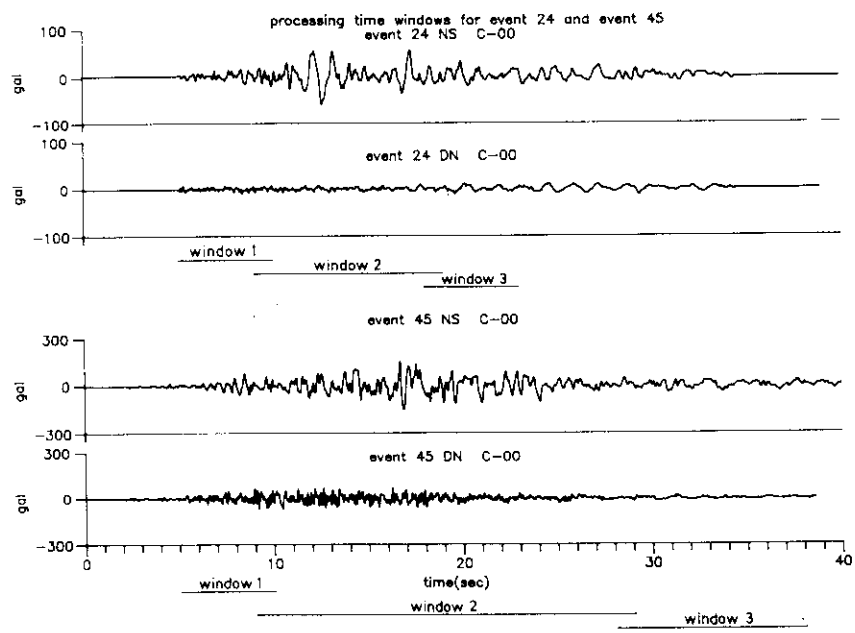

Fig. 3. Acceleration traces for events #24 and #45. Time windows used.

and rotational components [10,11], with respect to axes 1, 2, 3 as given by

$$u_m = d_m, \quad \dot{u}_m = v_m, \quad \text{and} \quad \ddot{u}_m = a_m,$$
$$u_{m+3} = \theta_m, \quad \dot{u}_{m+3} = \dot{\theta}_m, \quad \text{and} \quad \ddot{u}_{m+3} = \ddot{\theta}_m,$$
$$m = 1, 2, 3; \tag{1}$$

where d, v, and a denote displacement, velocity, and acceleration in the m direction, respectively, and where θ denotes rotation about the m axis. Both the time and frequency domain representations $u(t)$ and $U(i\bar{\omega})$ are complete and unique, where $U(i\bar{\omega})$ is the Fourier transform of $u(t)$. Displacement is treated herein as a function of both time and space, i.e., $u_m = u_m(t, x, y, z)$.

One direct way of analyzing data obtained at discrete locations on the ground surface is to compute the correlation function $R_{m,n}(t_0, \tau)$ between any two components u_m and u_n at locations i and j, respectively, as defined by

$$R_{m,n}(t_0, \tau) = \frac{1}{2\delta t} \int_{t_0 - \delta t}^{t_0 + \delta t} u_{mi}(t)\, u_{nj}(t+\tau)\, \mathrm{d}t. \tag{2}$$

For simplicity, let us first consider the same component of ground motion at each of the different locations. In this case, subscripts m and n can be dropped, leaving indices i and j to characterize the process. As will be seen later, this simplification does not diminish the generality of the subsequent development.

For a stationary random process, the cross correlation function depends only on the time lag τ, and it can be shown that

$$R_{ij}(\tau) = \int_{-\infty}^{\infty} S_{ij}(i\bar{\omega})\, e^{i\bar{\omega}\tau}\, \mathrm{d}\bar{\omega}, \tag{3}$$

where the function $S_{ij}(i\bar{\omega})$ given by

$$S_{ij}(i\bar{\omega}) = \lim_{T \to \infty} \frac{1}{2\pi T} \left[\int_{-T/2}^{T/2} u_i(t)\, e^{-i\bar{\omega}t}\, \mathrm{d}t \times \int_{-T/2}^{T/2} u_j(t)\, e^{+i\bar{\omega}t}\, \mathrm{d}t \right] \tag{4}$$

is called the cross power spectral density function between u_i and u_j. If $i = j$, eqs. (3) and (4) express the autocorrelation function $R_{ii}(\tau)$ and the power spectral density function $S_{ii}(\bar{\omega})$, respectively. Due to the nature of the process, $S_{ii}(\bar{\omega})$ is a real quantity, and $S_{ij}(i\bar{\omega})$ is a complex quantity having the properties $\mathrm{Re}(S_{ij}) = \mathrm{Re}(S_{ji})$ and $\mathrm{Im}(S_{ij}) = -\mathrm{Im}(S_{ji})$. This means that the matrix containing all spectral density functions $S_{ij}(i\bar{\omega})$ is Hermitian.

The cross correlation function $R_{ij}(\tau)$ can be normalized and be made dimensionless in accordance with the relation

$$\rho_{ij}(\tau) = \frac{R_{ij}(\tau)}{\sqrt{R_{ii}(0)}\sqrt{R_{jj}(0)}} \tag{5}$$

yielding a cross correlation coefficient $\rho_{ij}(\tau)$. The corresponding relation in the frequency domain is

$$\gamma_{ij}(i\bar{\omega}) = \frac{S_{ij}(i\bar{\omega})}{\sqrt{S_{ii}(\bar{\omega})}\sqrt{S_{jj}(\bar{\omega})}} \tag{6}$$

yielding a coherency function $\gamma_{ij}(i\bar{\omega})$. Both $\rho_{ij}(\tau)$ and $\gamma_{ij}^2(i\bar{\omega})$ – the coherence – are good indicators of the degree of correlation between two different signals. For totally correlated signals their corresponding values are ± 1 and 1, respectively, whereas for totally uncorrelated signals, their values are, in each case, zero. The time shift τ for which $\rho_{ij}(\tau)$ reaches its maximum value is related to the time that a given portion of the signal takes to travel from station i to station j. This shift in the time domain corresponds to a change $\exp(i\bar{\omega}\tau)$ in the frequency domain, where

$$\tau = d_{ij}^{\mathrm{L}}/v_{\mathrm{app}} \tag{7}$$

with v_{app} denoting the surface apparent wave velocity at frequency $\bar{\omega}$, and d_{ij}^{L} the projected separation distance in the longitudinal direction.

The concept of correlation and coherency can also be used to identify principal directions of propagation of given wave trains [12,5,6], and their degree of polarization [8]. To do so, the three dimensional characterization of wave propagation as measured at a given site should be considered. The reference Cartesian system for the travelling waves can be rotated into a position to produce, for a given time and frequency window, maximum values of ρ_{ij} and γ_{ij}^2. This is accomplished by determining the eigenvectors or principal directions of the matrices $R_{ij}(\tau = 0)$ or $\mathrm{Re}[S_{ij}(i\bar{\omega})]$, $i, j = 1, 2, 3$. In physical terms it means that, for a given time interval and frequency window, the particle motion can be described by a set of three independent orthogonal motions with peak amplitudes proportional to the axes of an ellipsoid. The ratios between pairs of eigenvalues which provide a measure of the degree of polarization of the corresponding motions, give the dimensions of the ellipsoid along principal axes. Using the coherency matrix approach, if the ratio is close to 1, it means that the wave is circularly polarized, and if close to zero, it is linearly polarized. This technique has been successfully

used in the identification of predominant wave trains, their directions of propagation, their apparent velocities, and their types of particle motion.

Using the so called F-K approach (frequency-wave number spectrum), Bolt et al. [5] and Abrahamson [6] identified predominant wave energy in the band 0.5–2.0 Hz propagating from the epicenter. Even though this technique is not as selective as the one developed by Loh and Penzien [13], the results are of the same order of magnitude.

More sophisticated treatments, such as stacking or the solution of a $3n$ (n being the total number of stations) eigenvalue problem, will extend the above mentioned concepts involving one station-pair to all stations in the array. Details of this type of analysis can be found elsewhere [8].

2.2. Data processing

In this investigation, systematic use has been made of the Fourier Spectrum and Frequency-Wave Number Spectrum Analysis [14], as tools to determine the main wave propagation characteristics. The direct and inverse FFT algorithms were used, after a DC removal, together with a 6-pole Butterworth band-pass filter applied in both the direct and reverse time axes to remove phase distortions. Corrected acceleration, velocity, and displacement time-histories were obtained using a low frequency cutoff at 0.1 Hz and a high frequency cutoff at 25.0 Hz. All integrations were carried out in the frequency domain. The results obtained using a 6-pole Butterworth filter were found to be very similar to the results obtained using the standard Ormsby filter used by the United States Geological Survey (USGS).

The Frequency-Wave Number Spectrum Analysis (F-K), was carried out using stacking high resolution array techniques [14], to compute the power for a given frequency window. The results provide information on wave numbers k_x and k_y which contain high power, and consequently, on both apparent velocity and azimuth of propagation. The existance of only one peak in the spectrum indicates the presence of a predominant plane wave. If several peaks exist, they indicate the presence of multiple waves propagating simultaneously at different apparent velocities along different azimuths.

While correlation functions were obtained directly in the time domain, the power spectral density and coherency functions were obtained in the frequency domain. The coherency computations required frequency smoothing prior to multiplication in order to obtain values different from 1. A triangular smoothing window with 9 points was used for this purpose.

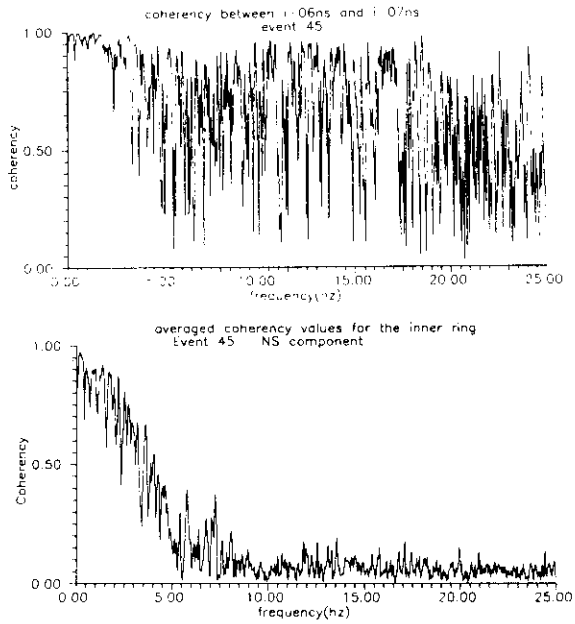

Fig. 4. Effect of averaging of coherency functions on noise reduction; (a, top) pair of stations, (b, bottom) average of 10 pairs of stations.

As mentioned in the previous section, spatial wave characterization can be made by using either the correlation coefficient function or the coherency function. In the present investigation, correlation coefficient functions were computed for many station pairs using different time and frequency windows. Results previously reported by Oliveira [7] shows, as expected, that the maximum values of the correlation coefficient functions are strongly dependent on the time and frequency windows used. The correlation coefficients, for the non-frequency filtered cases, were almost equal to one when the wave arrivals were well defined, e.g. using station pairs in the inner ring in the case of event No. 24. Elsewhere in the array the correlation coefficients dropped off to values of approximately 0.6. This technique permits the detection of the time shift τ for maximum correlation and, consequently, the evaluation of the corresponding apparent velocity. In those cases of low correlated signals, it is difficult by this technique to obtain good values of τ; therefore, other techniques such as the aligned phase spectrum method [15], is recommended. Frequency dependences which have been observed by others [16,6,15], are major factors controlling spatial correlation.

Working in the frequency domain, coherency is obtained through computation of the cross spectral den-

sity functions estimates S_{ij}. Based on his studies of SMART-1 data, Loh [16] suggested the following equation to compute S_{ij}:

$$S_{ij}(i\bar{\omega}) = S_0(\bar{\omega}) \mid \gamma_{ij}(\bar{\omega}) \mid \exp\left(i\bar{\omega} d_{ij}^{L}/v_{app}\right) \tag{8}$$

where

$$\mid \gamma_{ij}(\bar{\omega}) \mid = \exp\left(-\lambda \frac{\bar{\omega}}{2\pi} \mid d_{ij}^{L} \mid\right), \tag{9}$$

where λ is a frequency dependent parameter having units v^{-1} (v is velocity), v_{app} denotes the apparent wave velocity at frequency $\bar{\omega}$, and $S_0(\bar{\omega})$ is an averaged power spectral density function for the entire array. Selecting this form of equation was based on the observation that the cross spectrum attenuates with distance and experiences a phase shift due to the travelling waves. Also based on a study of the characteristics of four events, and assuming isotropy in loss of coherency with distance, Harichandran and Vanmarcke [15] suggested an equation of the form

$$\gamma_{ij}(i\bar{\omega}) = \left[A \exp\left(-\frac{2d_{ij}}{\alpha\theta(\bar{\omega})}(1 - A + \alpha A)\right) + (1 - A) \exp\left(-\frac{2d_{ij}}{\theta(\bar{\omega})}(1 - A + \alpha A)\right)\right] \times \exp\left(i\bar{\omega}\frac{d_{ij}^{L}}{v_{app}}\right), \tag{10}$$

where A and α are constants, $\theta(\bar{\omega})$ represents the spatial scale of fluctuation and d_{ij} is the distance between stations i and j. These parameters were all determined by the method of least squares using measured ground motion data. Using the data of event No. 20, Harichandran and Vanmarcke [15] obtained A, α, and the $\theta(\bar{\omega})$ function as given by

$$A = 0.736, \qquad \alpha = 0.147, \quad \text{and}$$

$$\theta(\bar{\omega}) = 3300\left[1 + \left(\frac{\bar{\omega}}{1.5\pi}\right)^{2}\right]^{-1/2}. \tag{11}$$

For engineering purposes one can use a simplified model for representing the travelling waves which consists of a single monochromatic wave propagating with a specified apparent velocity. This approach seems to give good results when considering displacements and it provides upper bound results when considering accelerations.

3. Estimation of model parameters based on SMART-1 array data

Model parameters, as described in section 2, were estimated using data recorded at the inner-ring stations of the SMART-1 array during events No. 24 and No. 45 following the procedure given below.

3.1. Coherency

Coherencies for all possible station pairs were obtained using the frequency domain approach (see section 2.2). As seen in fig. 4a, the coherency computed for each individual pair of stations shows a large noise content, which can be greatly reduced by averaging the coherencies of several station pairs. Fig. 4b shows how the averaging process of the amplitudes of the coherency functions for station pairs eliminates the presence of noise. To investigate the influence of noise in the coherency computations, white noise signals were generated, having absolute values of coherency for individual pairs of signals equal to approximately 0.3 over the entire frequency range considered. Averaging over many pairs greatly reduced this level of coherency.

In order to obtain a continuous function expressing loss of coherency with distance, station pairs having approximately the same projected separation distances (d_{ij}^{L}, d_{ij}^{T}) * were selected and categorized into nine groups (d_{ij}^{L}, d_{ij}^{T} = 50 m, 100 m, 200 m). Values of coherency loss for station pairs in each group were calculated and averaged. The averaged values, for which the noise had been substantially removed, were then used as the true values expressing loss of coherency between station pairs at the corresponding distances.

After considering the several models available in the literature which represent loss of coherency with distance [15–19], the present authors believe that a coherency function of the form

$$\gamma_{ij}\left(d_{ij}^{L}, d_{ij}^{T}, f\right) = \exp\left(-\beta_1 d_{ij}^{L} - \beta_2 d_{ij}^{T}\right) \times \exp\left[-\left(\alpha_1 d_{ij}^{L\,1/2} + \alpha_2 d_{ij}^{T\,1/2}\right) f^{2}\right] \times \exp\left(i\,2\pi f \frac{d_{ij}^{L}}{v_{app}}\right) \tag{12}$$

adequately represents field conditions. In this expression, f represents frequency in Hz ($\bar{\omega} = 2\omega f$), and the

* d_{ij}^{L} and d_{ij}^{T} are projected separation distances in the longitudinal direction of preferential wave propagation and in the transverse direction, respectively.

Table 2
Values of β_1 and β_2 for different components and events

	Event #24			Event #45		
	NS	EW	DN	NS	EW	DN
β_1	4.78×10^{-4}	same	5.1×10^{-4}	7.4×10^{-4}	same	1.88×10^{-4}
β_2	1.59×10^{-4}	same	2.64×10^{-4}	9.6×10^{-5}	same	3.43×10^{-5}

parameters β_1, β_2, α_1, and α_2 must be evaluated by the method of least square fitting using SMART-1 data; β_1 and β_2 were obtained by fitting the coherency values when $f=0$; however, α_1 and α_2 were computed to fit the coherency values at each frequency. Table 2 presents β_1 and β_2 for the different components and different events, and fig. 5 presents α_1 and α_2 as functions of frequency. In generating these parameters, the entire time-histories of ground motion were used, even though it was noticed that the frequency dependent coherency functions were somewhat time dependent. This dependency was judged to be too weak, however, to require a detailed time window analysis. As seen in fig. 5, the values for α_1 and α_2 show the coherency function to be much more dependent on longitudinal distance than on transverse distance; however, this observation did not hold for all components of motion, particularly in the lower frequency range. Fig. 6 shows the coherency values calculated by eq. (12) for different distances. As will be shown later in the generation of surface ground motions at the n site locations $(x_i, y_i, i=1, 2, \ldots, n)$, the developed algorithm requires the existence of both d_{ij}^{L} and d_{ij}^{T}.

Even though coherency values for distances greater than 400 m were not of much concern, their average values were computed for all stations in the middle and outer rings of the SMART-1 array having average separation values of 1000 m and 2000 m, respectively. Even these results were found to be in reasonable agreement with the coherency model presented above.

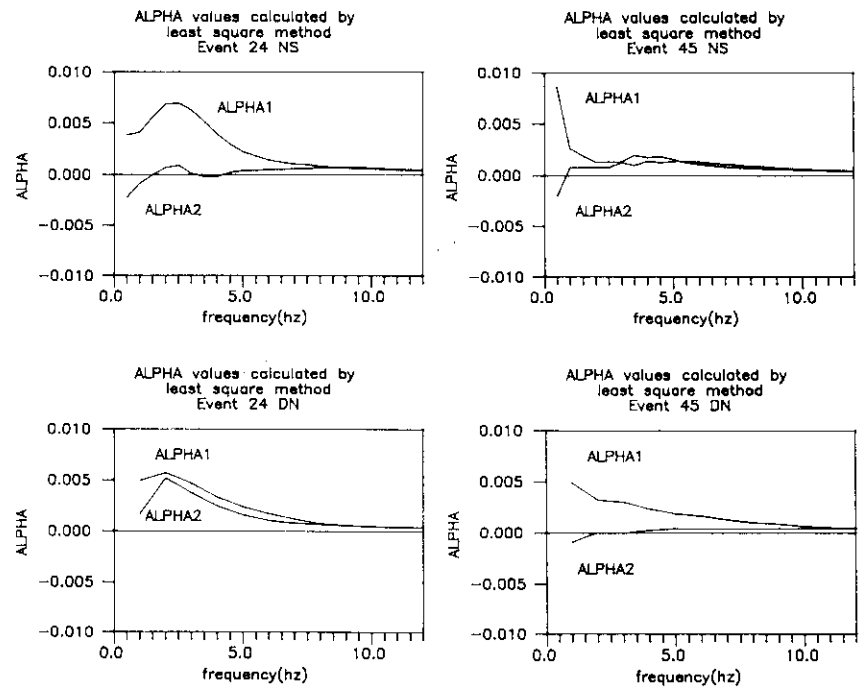

Fig. 5. Variation of α_1 and α_2 with frequency for different components and events.

Table 3
Parameter values for the Kanai-Tajimi power spectral density function for different time windows, components and events

Window	Event #24						Event #45					
	NS		EW		DN		NS		EW		DN	
	ξ_g	ω_g	ξ_g	ω_g	ξ_g	ω_g	ξ_g	ω_g	ξ_g	ω_g	ξ_g	ω_g
1	0.3	1.9	0.95	1.0			0.33	2.0	0.84	0.17	0.80	4.5
2	0.26	1.1	0.30	1.2			0.83	0.9	0.80	1.2	0.80	4.5
3	0.58	0.8	0.71	1.0			0.60	0.5	0.95	0.50	0.41	0.6

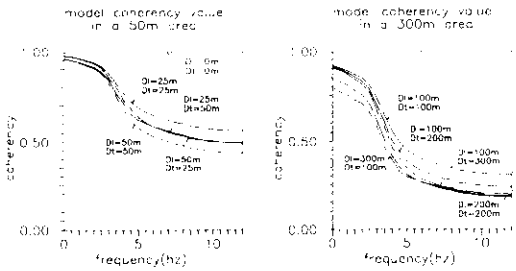

Fig. 6. Coherency function as derived by eq. (12) for different separation distances, d_{ij}^{L} and d_{ij}^{T}.

3.2. Power spectral density function

An averaged power spectral density function for all inner-ring stations was computed for each time window using the Kanai-Tajimi [20] form

$$S_0(\bar{\omega}) = \frac{\omega_g^4 + 4\xi_g^2\omega_g^2\bar{\omega}^2}{\left(\omega_g^2 - \bar{\omega}^2\right)^2 + 4\xi_g^2\omega_g^2\bar{\omega}^2} I. \tag{13}$$

The numerical values of constant ξ_g and ω_g obtained in each case are shown in table 3. The scaling factor I was found to have values as shown in table 4. Fig. 7 shows the averaged power spectral density functions for the inner-ring stations for different time windows. In only one case, namely the vertical component of event No. 24, did this Kanai-Tajimi form not correlate with field results. In this particular case, band-limited white noise was found to be more representative.

Table 4
Power spectrum scaling factors for different time windows, components and events

Window	Event #24			Event #45		
	NS	EW	DN	NS	EW	DN
1	1.0	1.0		1.0	1.0	0.42
2	1.34	0.94		1.49	1.24	0.42
3	1.65	1.06		2.07	1.8	1.21

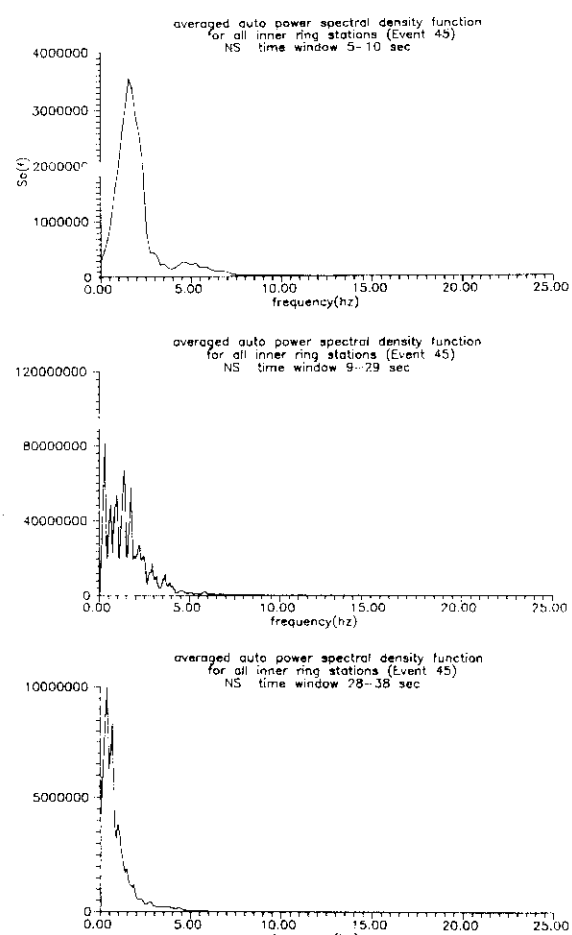

Fig. 7. Average power spectral density function for the inner-ring stations for different time windows.

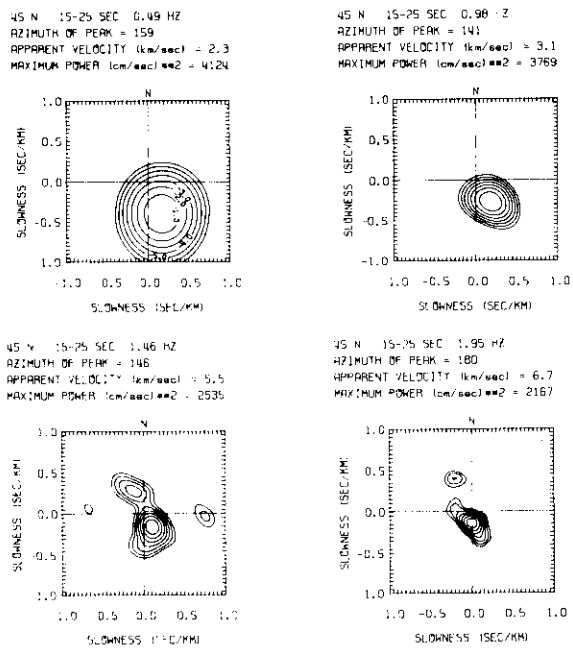

Fig. 8. Example of F-K spectrum to determine apparent velocity, azimuth of incoming waves and power.

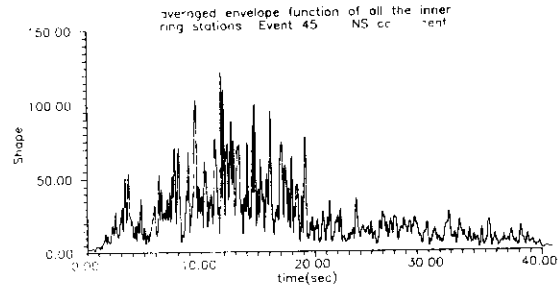

Fig. 10. Average shape function for the inner-ring stations.

3.3. Apparent velocity

Apparent velocity is the most difficult parameter to assess, even though preferential waves are propagating from the epicentral area to the site at all times. This difficulty is due to the presence of waves approaching from other directions with diverse apparent velocities which are particularly noticeable for frequencies above certain limits within the different time intervals. This feature, found to be present in all events, undoubtedly has characteristics reflecting the particular geological environment, where the waves are reflected and refracted in multiple forms. To illustrate the determina-

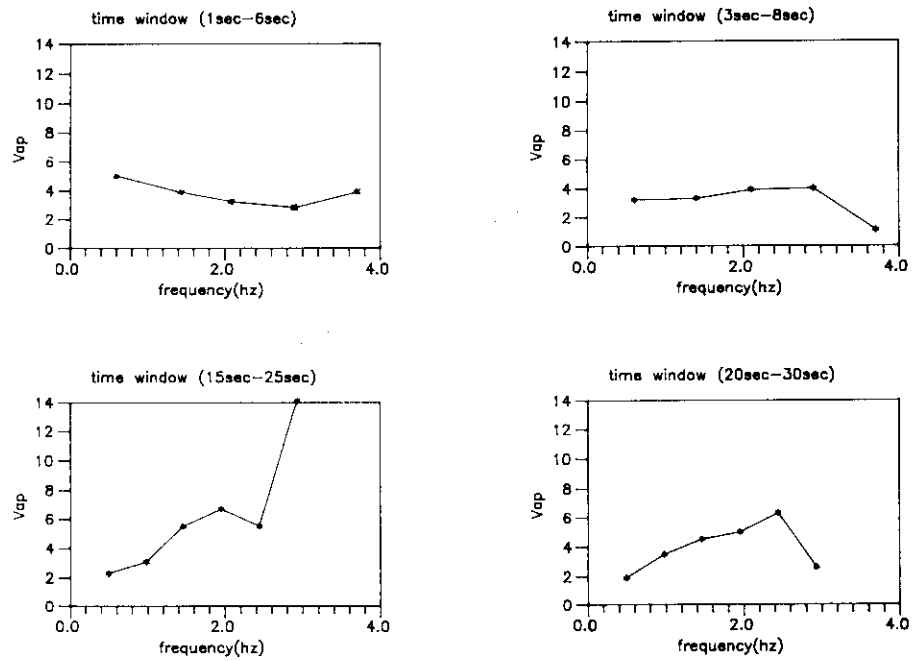

Fig. 9. Apparent velocities as a function of frequency.

tion of apparent velocity and azimuth of propagation, and F-K diagram of the approaching wave field for event No. 45, using a frequency window centered on $f = 0.49$ Hz, is shown in fig. 8. Fig. 9 shows the variations of apparent wave velocities with frequency for the different time windows.

Other techniques to detect apparent velocities and azimuth directions were also used such as the τ-x analysis [7] and the principle direction analysis [21]. Comparisons of the current results with those of other studies [16,15,21], show similar trends related to apparent velocity as a function of frequency.

3.4. Shape function

Hilbert transformations of the signals were used to determine the time envelope functions. For each component, average envelope functions were obtained for all inner-ring stations. Fig. 10 shows an example of the NS component for event No. 45. Based on the SMART-1 data, a shape function $\zeta(t)$ of the form

$$\zeta(t) = at \exp(-bt^2) \tag{14}$$

was found to correlate reasonably well except for the vertical components of motion recorded during event No. 24. In this case, a constant envelope intensity was found to be more appropriate throughout the entire time-history. The two parameters a and b in eq. (14) can be determined by normalizing the maximum value of $\zeta(t)$ to one at time t_0, which yields the relationships

$$t_0 = \frac{1}{\sqrt{2b}}, \quad a = \sqrt{2b}\,\mathrm{e} \quad \text{and} \quad \zeta(t_0) = 1.0, \tag{15}$$

where e is the base of the natural logarithm. Table 5 shows the values of a and b for different components and different events.

3.5. Coherency among different components at the same station

Coherency between the horizontal components recorded at each station was computed station by station,

Table 5
Shape function paremeter values for different components and events

	#24			#45		
	NS	EW	DN	NS	EW	DN
t_{max}(s)	8	11		12	12	8
a	0.206	0.15		0.1374	0.1374	0.206
b	0.0078	0.00413		0.00347	0.00347	0.0078

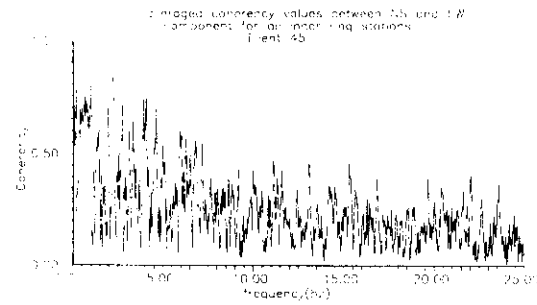

Fig. 11. Average coherency function for different components at the same station.

and then, the average was obtained for all stations. Fig. 11 shows the results obtained for event No. 45 between the NS and Ew components. The low values shown indicate that correlation among horizontal components is very small as one would have expected because the NS direction is nearly the same as epicentral direction which normally is close to being the direction of major principal motion.

4. Simulation of strong ground motion

4.1. Ground motion generation in the time domain

Assuming that earthquake ground motions are stationary random processes having zero mean values and known power spectral density functions and cross coherency functions, a series of spatially correlated ground motions can be generated through the following method [23]:

Assume the ground motion time series have the same power spectral density function $S_0(\bar{\omega})$ ($-\bar{\omega}_N \le \bar{\omega} \le \bar{\omega}_N$, where $\bar{\omega}_N$ is the Nyquist frequency) at every station, which is a reasonable approach when the focus of the earthquake is at a large distance from the site as compared to the site dimension. The cross power spectral density functions $S_{ij}(i\bar{\omega})$ can now be expressed in terms of $S_0(\bar{\omega})$ and the coherency functions $\gamma_{ij}(i\bar{\omega})$ as given by

$$\boldsymbol{S}(\bar{\omega}) = \begin{bmatrix} \gamma_{11}(\bar{\omega}) & \gamma_{12}(i\bar{\omega}) & \cdots & \gamma_{1n}(i\omega) \\ \gamma_{21}(i\bar{\omega}) & \gamma_{22}(\bar{\omega}) & \cdots & \gamma_{2n}(i\bar{\omega}) \\ \cdots & \cdots & \cdots & \cdots \\ \gamma_{n1}(i\omega) & \gamma_{n2}(i\bar{\omega}) & \cdots & \gamma_{nn}(\bar{\omega}) \end{bmatrix} S_0(\bar{\omega}),$$

$$-\bar{\omega}_N \le \bar{\omega} \le \bar{\omega}_N. \tag{16}$$

The generated time series $u_1(t)$, $u_2(t)$, ..., $u_n(t)$, must

be compatible with the individual functions in $\boldsymbol{S}(\bar{\omega})$. To do this, let

$$u_i(t) = \sum_{m=1}^{i} \sum_{n=1}^{N} A_{im}(\bar{\omega}_n) \times \cos\left[\bar{\omega}_n t + \beta_{im}(\bar{\omega}_n) + \phi_{mn}(\bar{\omega}_n)\right], \tag{17}$$

where amplitudes $A_{im}(\bar{\omega}_n)$ and phase angles $\beta_{im}(\bar{\omega}_n)$ are to be determined to insure the proper correlation relations satisfying eq. (16), and $\phi_{mn}(\bar{\omega}_n)$ is a random phase angle uniformly distributed over the range zero to 2π. Note ϕ_{mn} and ϕ_{rs} should be statistically independent unless $m = r$, and $n = s$.

To obtain the proper values of $A_{im}(\bar{\omega})$ and $\beta_{im}(\bar{\omega})$ at each discrete frequency $\bar{\omega}_n$, the contribution to the time average $\langle u_i(t)u_j(t)\rangle$, by $u_i(t)$ and $u_j(t)$ in a frequency band $\Delta\bar{\omega}$ centered on $\bar{\omega}_n$ is considered. Assume $i \geq j$; then for motion in this frequency band, the time average is

$$\langle u_{in}(t)u_{jn}(t)\rangle = \left\langle \left\{ \sum_{m=1}^{i} A_{im}\cos(\bar{\omega}_n t + \beta_{im} + \phi_{mn}) \right\} \times \left\{ \sum_{r=1}^{j} A_{jr}\cos(\bar{\omega}_n t + \beta_{jr} + \phi_{rn}) \right\} \right\rangle, \tag{18}$$

when $m > j$ and $m \neq r$, $\langle u_{in}(t)u_{jn}(t)\rangle = 0$ since in these cases, ϕ_{mn} and ϕ_{rn} are statistically independent. The above equation then reduces to

$$\begin{aligned}\langle u_{in}(t)u_{jn}(t)\rangle &= \left\langle \sum_{m=1}^{j} A_{im}A_{jm}\cos(\bar{\omega}_n t + \beta_{im} + \phi_{mn}) \times \cos(\bar{\omega}_n t + \beta_{jm} + \phi_{mn}) \right\rangle \\ &= \sum_{m=1}^{j} \frac{A_{im}A_{jm}}{2} \langle \cos(2\bar{\omega}_n t + \beta_{im} + \beta_{jm} + 2\phi_{mn}) + \cos(\beta_{im} - \beta_{jm}) \rangle \\ &= \sum_{m=1}^{j} \frac{A_{im}A_{jm}}{2} \cos(\beta_{im} - \beta_{jm}), \quad n = 1, 2, \ldots, N.\end{aligned} \tag{19}$$

The cross power spectral density function $S_{ij}(i\bar{\omega})$ has the properties that its real and imaginary parts are even and odd, respectively; thus, the corresponding amplitude function $A_{ij}(\bar{\omega})$ is even, and the phase angle function $\beta_{ij}(\bar{\omega})$ is odd. Hence, the above time average for discrete harmonic $\bar{\omega}_n$ can be expressed as

$$\begin{aligned}\langle u_{in}(t)u_{jn}(t)\rangle &= \mathrm{Re}\left[\sum_{m=1}^{j} \frac{A_{im}A_{jm}}{2} e^{i(\beta_{im}-\beta_{jm})} \right] \\ &= \mathrm{Re}\left[\sum_{m=1}^{j} \tfrac{1}{2} H_{im}(i\bar{\omega}_n) H_{jm}^{*}(i\bar{\omega}_n) \right], \\ n &= 1, 2, \ldots, N;\end{aligned} \tag{20}$$

where Re denotes real part, $H_{im}(i\bar{\omega}_n) = A_{im}(\bar{\omega}_n) \times e^{i\beta_{im}(\bar{\omega}_n)}$, and the superscript * means complex conjugate.

The above time average at frequency $\bar{\omega}_n$ over the band width $\Delta\bar{\omega}$ can also be expressed in terms of the spectral density functions in the form

$$\begin{aligned}&\langle u_{in}(t)u_{jn}(t)\rangle \\ &= S_{ij}(i\bar{\omega}_n)\,\Delta\bar{\omega} = S_0(\bar{\omega}_n)\left[\gamma_{ij}(i\bar{\omega}_n) + \gamma_{ij}(-i\bar{\omega}_n)\right]\Delta\bar{\omega} \\ &= \mathrm{Re}\left[2S_0(\bar{\omega}_n)\gamma_{ij}(i\bar{\omega}_n)\right]\Delta\omega = \mathrm{Re}\left[2S_{ij}(i\bar{\omega}_n)\right]\Delta\omega, \\ &n = 1, 2, \ldots, N.\end{aligned} \tag{21}$$

Since matrix $\boldsymbol{S}(\bar{\omega})$ given by eq. (16) is Hermitian and positive definite, it can always be decomposed into the multiplication of a complex lower triangular matrix $\boldsymbol{L}(i\bar{\omega}_n)$ and its Hermitian $\boldsymbol{L}^{H}(i\bar{\omega}_n)$ [24], as shown by

$$\boldsymbol{S}(\bar{\omega}) = \boldsymbol{L}(i\bar{\omega})\boldsymbol{L}^{H}(i\bar{\omega})S_0(\omega), \tag{22}$$

where

$$\boldsymbol{L}(i\bar{\omega}) = \begin{bmatrix} l_{11}(\bar{\omega}) & 0 & \ldots & 0 \\ l_{21}(i\bar{\omega}) & l_{22}(\bar{\omega}) & \ldots & 0 \\ \ldots & \ldots & \ldots & \ldots \\ l_{n1}(i\bar{\omega}) & l_{n2}(i\bar{\omega}) & \ldots & l_{nn}(\bar{\omega}) \end{bmatrix} \tag{23}$$

and where l_{ij} $(i = 1, 2, \ldots, n,\ j = 1, 2, \ldots, i)$ can be calculated by the Cholesky method [25],

$$l_{ii}(\bar{\omega}) = \left[\gamma_{ii}(\bar{\omega}) - \sum_{k=1}^{i-1} l_{ik}(i\bar{\omega})l_{ik}^{*}(i\bar{\omega})\right]^{1/2}, \quad i = 1, 2, \ldots, n; \tag{24}$$

$$l_{ij}(i\bar{\omega}) = \frac{\gamma_{ij}(i\bar{\omega}) - \sum_{k=1}^{j-1} l_{ik}(i\bar{\omega})l_{jk}^{*}(i\bar{\omega})}{l_{jj}(\bar{\omega})}, \quad j = 1, 2, \ldots, i. \tag{25}$$

For the case $i \geq j$, the individual functions in $\boldsymbol{S}(\bar{\omega})$ can be written as

$$S_{ij}(\mathrm{i}\bar{\omega}_n) = 2S_0(\bar{\omega}_n) \sum_{m=1}^{j} L_{im}(\mathrm{i}\bar{\omega}_n) L_{jm}^*(\mathrm{i}\bar{\omega}_n)\ \Delta\omega,$$
$$n = 1, 2, \ldots, N. \tag{26}$$

Equating eqs. (20) and (21), the following expressions are obtained

$$A_{ij}(\bar{\omega}) = \sqrt{4S_0(\bar{\omega})\ \Delta\omega}\ |l_{ij}(\mathrm{i}\bar{\omega})|, \quad 0 \leq \bar{\omega} \leq \bar{\omega}_N;$$
$$\beta_{ij}(\bar{\omega}) = \tan^{-1}\left(\frac{\mathrm{Im}[l_{ij}(\mathrm{i}\bar{\omega})]}{\mathrm{Re}[l_{ij}(\mathrm{i}\bar{\omega})]}\right), \quad 0 \leq \bar{\omega} \leq \bar{\omega}_N. \tag{27}$$

Making use of eqs. (17) and (27), a set of spatially correlated time series $u_i(t)$ $(i = 1, 2, \ldots, n)$ can be generated, and the corresponding ground motions $a_i(t)$ $(i = 1, 2, \ldots, n)$ can be obtained by multiplying each time series by a proper shape function $\zeta(t)$. By this procedure, one first generates a time series for site 1, then for site 2 by summing up wave contributions that are properly correlated with the first one. Similarly, the generated time series for site 3 will be correlated with those previously generated for both sites 1 and 2, etc. The first time series can be either a synthetic motion or a real motion provided it is compatible with the prescribed spectral density matrix $S_0(\bar{\omega})$.

4.2. Ground motion generation in the frequency domain

Ground motions can be generated more easily in the frequency domain than in the time domain by using eq. (17). To proceed with this new approach, express the Fourier transform of $u_i(t)$ in the form

$$U_i(\mathrm{i}\bar{\omega}_n) = \sum_{m=1}^{i} B_{im}(\bar{\omega}_n)[\cos\alpha_{im}(\bar{\omega}_n) + \mathrm{i}\sin\alpha_{im}(\bar{\omega}_n)],$$
$$n = 1, 2, \ldots, N; \tag{28}$$

where $B_{im}(\bar{\omega}_n)$ is the amplitude at frequency $\bar{\omega}_n$, and $\alpha_{im}(\bar{\omega}_n)$ is the corresponding phase angle. By transforming eq. (17) into the frequency domain, it can be shown that

$$B_{im}(\bar{\omega}_n) = A_{im}(\bar{\omega}_n)/2,$$
$$\alpha_{im}(\bar{\omega}_n) = \beta_{im}(\bar{\omega}_n) + \phi_{mn}. \tag{29}$$

Then, using eqs. (29) and (27), $U_i(\mathrm{i}\bar{\omega}_n)$ as expressed in eq. (28) becomes fully known; thus, the corresponding time series $u_i(t)$ can be obtained by inverse transforming $U_i(\mathrm{i}\bar{\omega}_n)$ back into the time domain.

4.3. Response spectrum compatible time series

It is common practice in engineering to specify the design earthquake ground motions through the standard response spectrum, say $S_v(\omega, \xi)$ which denotes the pseudo velocity response spectrum for the single degree of freedom system having a natural frequency ω and a damping ratio ξ. In this case, it is necessary to adjust the generated ground acceleration time-history $a_i(t)$ so that it is compatible with the prescribed response spectrum $S_v(\omega, \xi)$. If $A_i(\mathrm{i}\bar{\omega})$ is the Fourier transform of $a_i(t)$, the first adjustment can be made by multiplying $A_i(\mathrm{i}\bar{\omega})$ by the ratio $S_v(\omega = \bar{\omega}, \xi)/\hat{S}_v(\omega = \bar{\omega}, \xi)$, where $\hat{S}_v(\omega, \xi)$ is the actual response spectrum for $a_i(t)$, and then inverse Fourier transforming the product back to the time domain to get an adjusted accelerogram $\hat{a}_i(t)$. This adjustment procedure can be repeated as necessary to make the final resulting accelerogram spectrum compatible to the degree required. The number of adjustments required increases with the damping ratio ξ; however for the commonly used ratio $\xi = 0.05$, only two or three adjustments are needed. Note that in this adjustment procedure, only the Fourier amplitudes of $a_i(t)$ are changed, i.e. their phase angles remain unchanged. Because the phase angles remain unchanged, the correlation coefficient between $a_i(t)$ and $a_j(t)$ will be the same as between $\hat{a}_i(t)$ and $\hat{a}_j(t)$. Also the coherency function will not change with this adjustment if no smoothing operation is applied when computing the coherency. If smoothing is applied some change will be found depending on the smoothing window length. In one example, two time series were generated and adjusted to be compatible with the same response spectrum. It was found that the coherency, which was computed with a smoothing window of bandwidth 0.22 Hz, remained nearly the same showing a good match with the specified model.

4.4. Quasi-stationary power spectral density function

Earthquake records, such as those obtained at the SMART-1 array, show a tendency for non-stationarity in both the time and frequency domains. In recognition of these tendencies, the non-stationary in the time domain can be easily modelled by multiplying each stationary accelerogram by an appropriate shape function. To represent quasi-stationarity in the frequency domain, the total duration of ground motion is divided into separate segments of stationary motion having

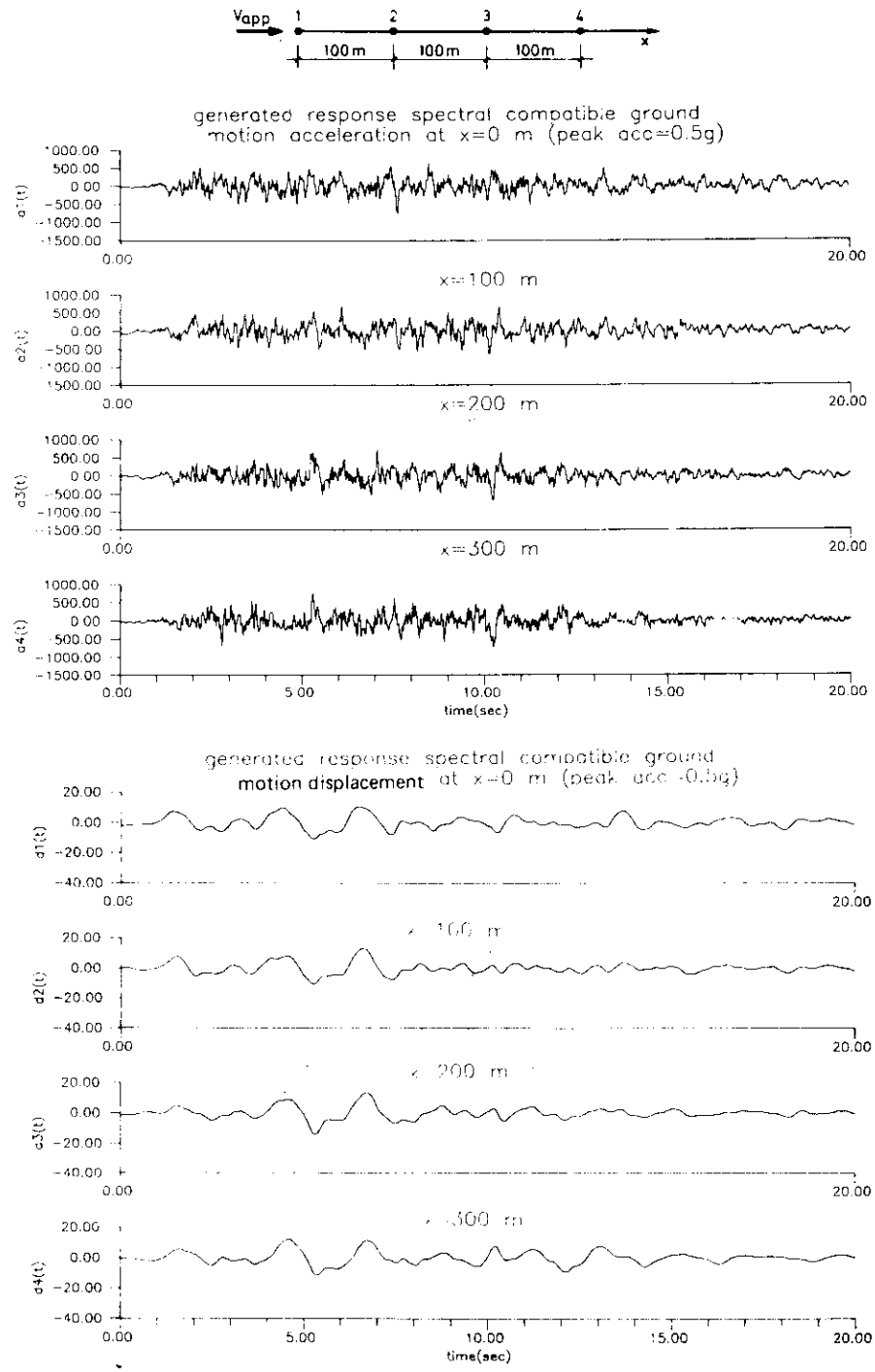

Fig. 12. Example of generated ground motions for several sites located along a straight line; (a, top) acceleration, (b, bottom) displacement.

different power spectral density representations. In order to render continuity at the beginning and end of each segment, an overlapping of time windows is used along with a specified transitional weighting function.

5. Applications

Two examples were chosen to test the algorithm developed. The first one deals with the generation of stationary ground motions for several sites along a straight line. The second example deals with the generation of quasi-stationary ground motions for a 2-D network of stations.

5.1. Example No. 1

Spatially correlated ground motion time series were generated for four locations spaced at 100 m intervals ($d = 0$; 100; 200; 300 m) along the direction of wave propagation. In this example, the Kanai-Tajimi power spectral density function with $\xi_g = 0.6$ and $\omega_g = 2.5$ Hz, eq. (13); the Harichandran and Vanmarcke coherency function, eq. (10), with $A = 0.736$, $\alpha = 0.147$, and $v_{app} = 2.5$ km/s; and the commonly used Jennings shape function of the form

$$\zeta(t) = \begin{cases} (t/t_0)^2 & \text{for} \quad 0 \le t \le t_0, \\ 1 & \text{for} \quad t_0 \le t \le t_n, \\ \exp[-0.155(t - t_n)] & \text{for} \quad t_n \le t \end{cases} \tag{30}$$

with $t_0 = 2$ s and $t_n = 10$ s were used. After generation of the four time series, the Newmark and Hall [26] design response spectrum normalized to $0.5g$ peak ground acceleration for a damping ratio $\xi = 0.05$ was chosen as the specified response spectrum.

The four generated ground motion time series are shown in figs. 12a and 12b, respectively for acceleration and displacement. Fig. 13 presents the cross correlation coefficient for motions at stations 1-2, 2-3 and 1-4; fig. 14 presents the corresponding coherency function; fig. 15 presents the power spectral density function; and fig. 16 presents the actual response spectra where they can be compared with the prescribed Newmark and Hall spectrum. Based on these results, certain observations can be made as follows:

(1) The basic features of wave propagation are observed in the four time series. Cross correlations of the acceleration traces show peak values in agreement with the specified apparent velocity. The peak values of cross correlation coefficient obtained were 0.6 at 100 m, 0.61 at 200 m, and 0.38 at 300 m. Displacement traces, show very high correlated shapes, as expected.

(2) The power spectral density functions match well the specified Kanai-Tajimi spectral density function. The apparent discrepancies with high values as observed in fig. 15 for $d = 300$ m in the lower frequency portion of the spectrum, may be attributed to certain random features of the process. For other time series generated, these discrepancies did not repeat.

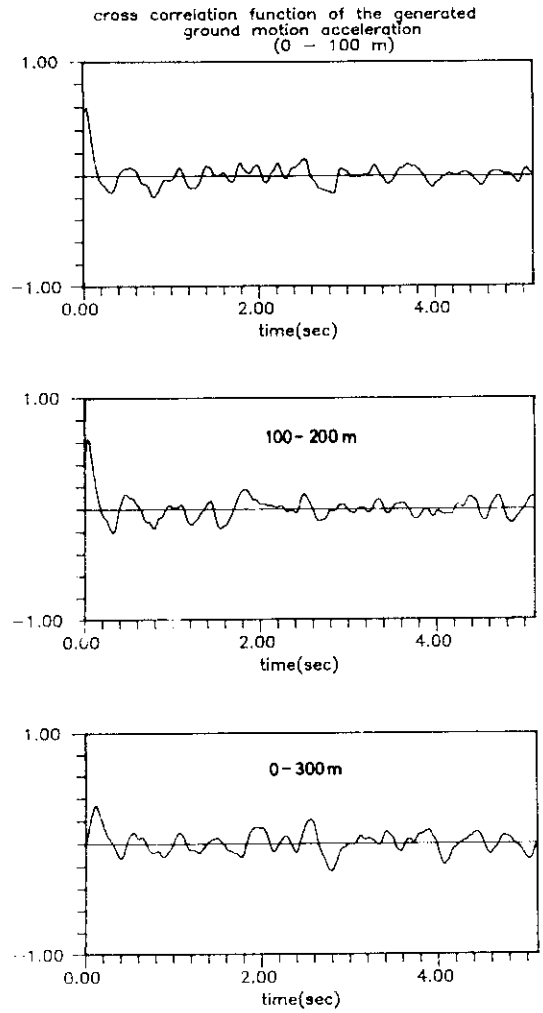

Fig. 13. Cross correlation function of the generated ground motion.

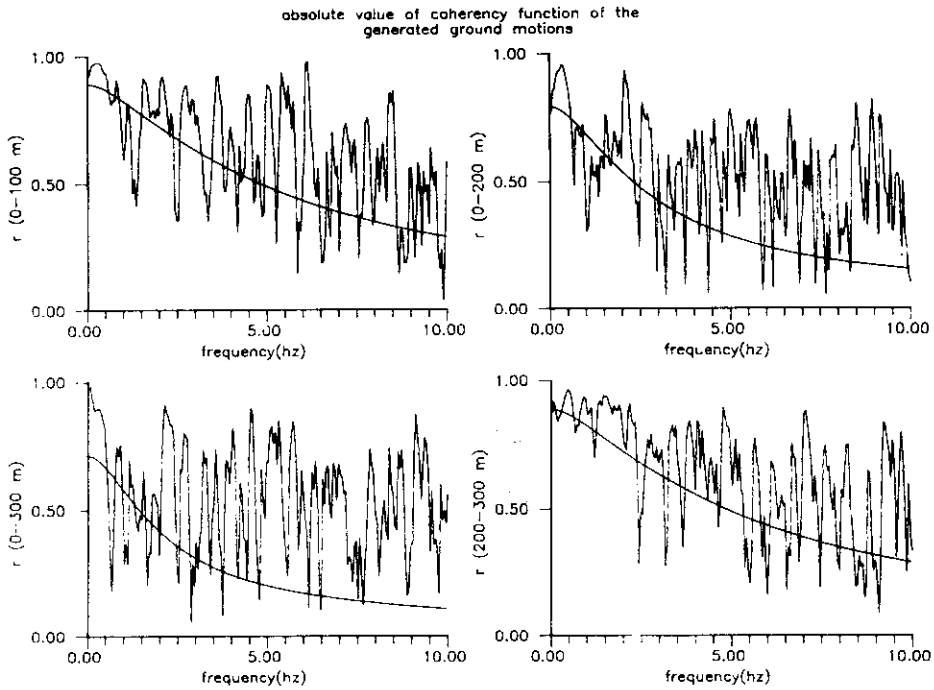

Fig. 14. Coherency function of the generated ground motion. Comparison with model.

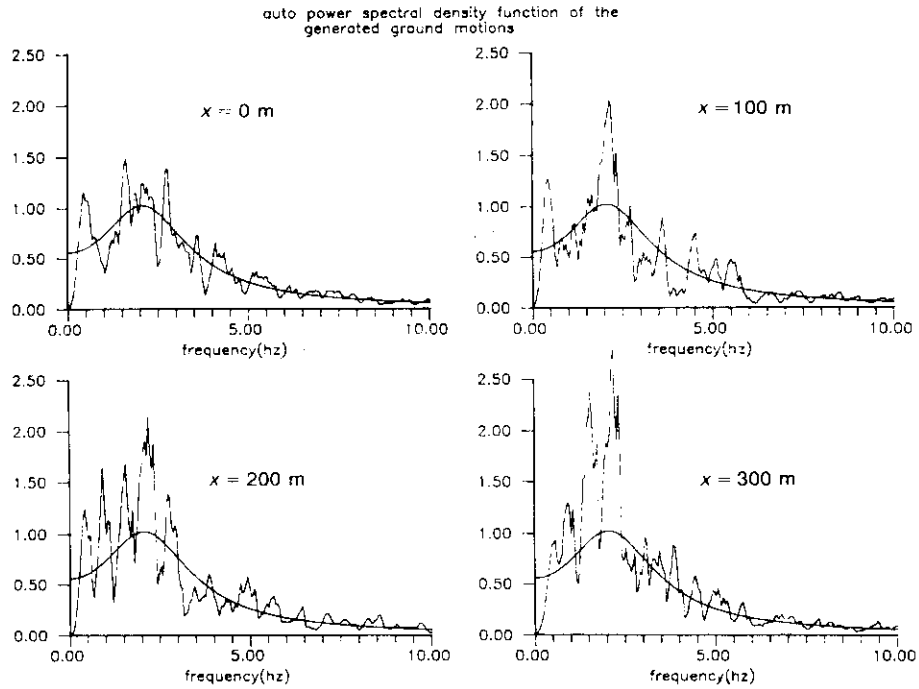

Fig. 15. Power spectral density function of generated ground motion. Comparison with model.

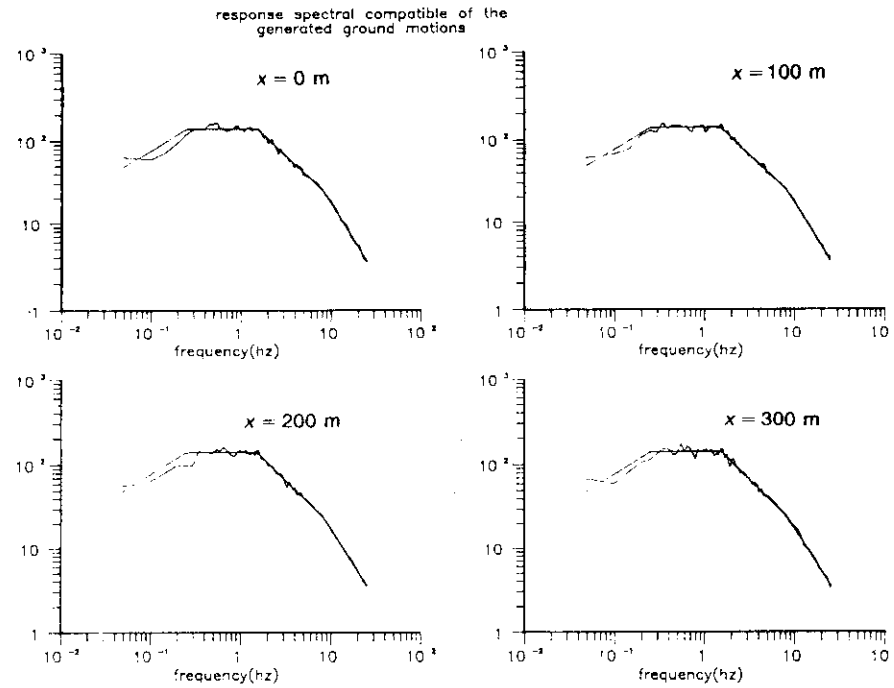

Fig. 16. Spectra compatible generated ground motion.

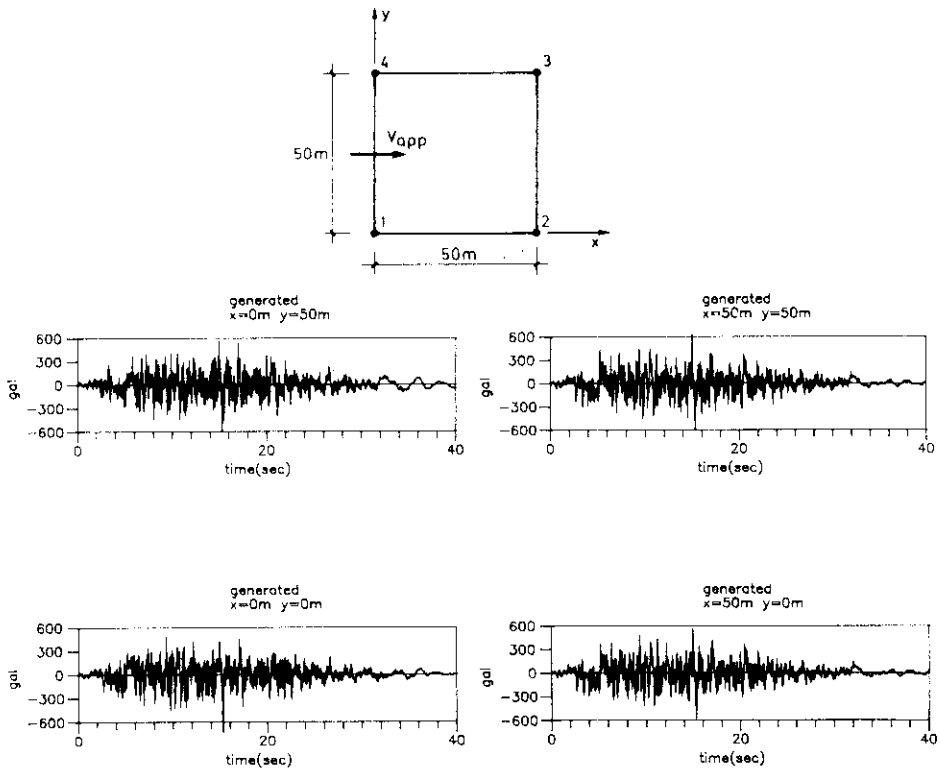

Fig. 17. Example of generated ground motion for a two-dimensional network of stations.

(3) The coherency functions also are in good ag ement with the specified Harichandran and Vanmarcke coherency model as can be seen in fig. 14.

5.2. Example No. 2

In example No. 2, ground motions were generated for stations located in a 2-D site. Four time series were generated at the four corners of a 50 m square site. The results obtained by processing the SMART-1 data for event No. 45 were used. The four time series of 40 s duration and $\Delta t = 0.02$ s, fig. 17, exhibit characteristics similar to the time series recorded at the SMART-1 array for event No. 45 (section 3). The following functions were used in generating the acceleration time histories:

(1) The coherency function suggested by the present authors as given by eq. (12) with the parameters of table 2 was used. The apparent velocity was assumed, for simplicity, as being constant and equal to $v_{app} = 3.5$ km/s, and the waves were assumed to be propagating in the positive x-direction.
(2) Three power spectral density functions of the Kanai-Tajimi form were used for three time windows (1st window 0–5 s; 2nd window 4–32 s; 3rd window 31–40 s). These spectral density functions had parameters as given in tables 3 and 4 representing the NS components recorded during event No. 45.
(4) The shape function given by eq. (14) with the parameters of table 5 representing the NS components of event No. 45 was used.

An analysis of the four acceleration time series presented in fig. 17 shows the following:

(1) The basic features of propagation are observed in the four time series. Computed cross correlations, coherency and power spectral density functions are in good agreement with the prescribed model defined above.
(2) The overall features of the time series resemble quite well those of the real time series. The variability of peak ground accelerations among the four records (average value of $0.6g$) is within the limits of measured values [27].

6. Concluding statements

A coherency model of nonisotropic form for components of motion at multiple stations is developed herein which is believed to have a general application. Further, a simple numerical procedure is presented which allows the generation of time series which are compatible with this model and are also compatible with any specified design response spectrum.

Acknowledgements

This paper presents the results of research carried during 1987 at the Seismographic Station, University of California, Berkeley, which was supported by the National Science Foundation under Grant No. ECE-8417856. The authors express their sincere thanks and appreciation to Dr. B.A. Bolt, Director of the Seismographic Station, for his support and encouragement during the entire study. The F-K computer software made available through the Seismographic Station by Drs. N.A. Abrahamson and R.D. Darragh and specialized assistance provided by S.J. Chiou, are greatly acknowledged.

Nomenclature

$R_{ij}(\tau)$	correlation function,
$S_{ij}(i\bar{\omega})$	cross spectral density function,
$\rho_{ij}(\tau)$	correlation coefficient,
$\gamma_{ij}(\bar{\omega})$	coherency function,
d_{ij}^{L}	separation distance projected in the longitudinal direction of propagation,
d_{ij}^{T}	separation distance projected in the transverse direction of propagation,
v_{app}	apparent velocity,
F-K	frequency-wave number spectrum,
f	frequency in Hz,
$\bar{\omega}$	frequency in rad/s,
k_x	wave number of the x-direction,
k_y	wave number ih the y-direction,
$S_0(\bar{\omega})$	power spectral density function,
ω_g, ξ_g	Kanai-Tajimi parameters values,
Γ	scaling factor,
α_1, α_2, β_1, β_2	coherency parameters values,
$\xi(t)$	shape function,
$S_v(\omega, \xi)$	pseudo-velocity response spectrum for frequency ω and damping ratio ξ.

References

[1] N.M. Newmark and E. Rosenblueth, Fundamentals of Earthquake Engineering (Prentice Hall, Englewood Cliffs, NJ, 1971).
[2] J.P. Wolf, P. Obernhuber and B. Weber, Response of a nuclear power plant on aseismic bearings to horizontal

propagating waves, Earthq. Engrg. and Str. Dyn. 11 (1983) 483–499.

[3] R.T. Duarte, Spatially variable ground motion models for the earthquake design of bridges and other extended structures, 8th World Conf. Earthq. Engrg., Vol II, pp. 613–620 (Prentice Hall, Englewood Cliffs, NJ, 1984).

[4] J.E. Luco, Response of a rigid foundation to a spatially random ground motion, Earthq. Engrg. and Str. Dyn. 14 (1986) 891–908.

[5] B.A. Bolt, C.H. Loh, J. Penzien, Y.B. Tsai and Y.T. Yeh, Preliminary Report on the SMART-1 strong motion array in Taiwan, Report UBC/EERC-82/13, University of California, Berkeley (1982).

[6] N.A. Abrahamson, Estimation of seismic wave coherency and rupture velocity using the SMART-1 strong motion array recordings, Report UCB/EERC-85/2, University of California, Berkeley (1985).

[7] C.S. Oliveira, Variability of strong ground motion characteristics obtained in SMART-1 array, Proc. 12th Regional Seminar on Earthquake Engineering, Halkidiki, Greece (1985).

[8] R.B. Darragh, Analysis of the near-source waves: Separation of wave types using strong motion array recordings, PhD Thesis, University of California, Berkeley (1987).

[9] B.A. Bolt and S.J. Chiou, Strong motion array analysis of the November 14, 1986 Taiwan earthquake, Personal Communication (1987).

[10] J. Penzien, Lecture notes on earthquake engineering analysis, University of California, Berkeley (1985).

[11] C.S. Oliveira, Probabilistic assessment of strong ground motion, in: Strong Motion Seismology, Eds. M.O. Erdik and M.N. Toksoz, Series C: Mathematical and Physical Sciences, Vol. 204, pp. 405–460 (D. Reidel Publishing Co., Dordrecht, Holland, 1987).

[12] C.H. Loh, J. Penzien and Y.B. Tsai, Engineering analysis of SMART-1 array accelerograms, Earthq. Engrg. and Str. Dyn. 10 (1982) 575–591.

[13] C.H. Loh and J. Penzien, Identification of wave types, directions, and velocities using SMART-1 strong motion array data, 8th World Conf. Earthq. Engrg., Vol II, pp. 191–198 (Prentice Hall, Englewood Cliffs, NJ, 1984).

[14] N.A. Abrahamson and B.A. Bolt, Array analysis and synthesis mapping of strong seismic motion, in: Strong Motion Synthetics, Ed. B.A. Bolt, pp. 55–90 (Academic Press, Orlando, 1987).

[15] R. Harichandran and E. Vanmarcke, Space-time variation of earthquake ground motion, Research Report R84-12, Dept. Civil Engrg., Massachusetts Institute of Technology (1984).

[16] C.H. Loh, Analysis of the spatial variation of seismic waves and ground movements for SMART-1 array data, Earthq. Engrg. and Str. Dyn. 13 (1985) 561–581.

[17] A. Mita and J.E. Luko, Response of structures to a spatially random ground motion, 3rd US National Conf. on Earthq. Engrg., pp. 907–918, Charleston, USA (1986).

[18] N.A. Abrahamson, Coherency analysis of strong ground motion, Personal communication (1988).

[19] Y.B. Tsai, Empirical characterization of free-field ground motion for soil–structure interaction analysis, 2nd Workshop on Strong Motion Arrays, Taipei (1988).

[20] K. Kanai, An empirical formula for the spectrum of strong earthquake motions, Bull. Earthq. Res. Inst., University of Tokyo, Vol. 39 (1961).

[21] J. Penzien and M. Watabe, Characteristics of 3-dimensional earthquake ground motions, Earthq. Engrg. and Str. Dyn. 3 (1975) 365–373.

[22] Y. Fukumori, M. Sato, T. Kikuta, K. Yanabu and K. Toki Detection of dispersion characteristics of apparent wave velocity, 8th World Conf. Earthq. Engrg., Vol II, pp. 223–230 (Prentice Hall, Englewood Cliffs, NJ, 1984).

[23] E. Samaras, M. Shinozuka and A. Tsurui, Time series generation using the autoregressive moving average model, in: Stochastic Mechanics, Ed. M. Shinozuka, Dep. Civil Engrg. and Engrg. Mechanics, Columbia University, Vol II, pp. 1–130, New York (1987).

[24] F.R. Gantmacher, The Theory of Matrices (Chelsea Publishing Company, NY, 1977).

[25] K.E. Atkinson, An Introduction to Numerical Analysis (John Wiley and Sons, NY, 1978).

[26] N.M. Newmark and W.J. Hall, Seismic design criteria for nuclear reactor facilities, 4th World Conf. Earthq. Engrg., Vol II, pp. B4/37-B4/50, Santiago, Chile (1969).

[27] C.S. Oliveira, F. Pimentel and J. Azevedo, Variability of strong ground motion ordered peaks at a site based on dense seismic arrays, 8th Europ. Conf. Earthq. Engrg., Vol. 6, Lisbon, Portugal (1986).

3-D VISUALIZATION OF EARTHQUAKE WAVE PROPAGATION ACROSS SMART-1 ARRAY

Carlos S. Oliveira[1],M.EERI and Anthony J.H. Lomax[2]

The SMART-1 strong motion array provides an unique opportunity to visualize wave propagation across 37 closely located surface stations. In this paper we describe the capabilities of the graphics software tool which produces a set of instantaneous images of the deformation of the surface layer. Secondly, we show how these images can be useful in identifying some important features of global 2-D or 3-D patterns of strong motion wave propagation. Finally, we stress the importance of wave visualization as an educational tool.

EXCERTS

INTRODUCTION

The direct visual observation of earthquake wave propagation has always been a curiosity of human kind. Surface undulations in the landscape produced by incoming waves is among one of the common reported accounts in early written reports describing the effects of earthquake motion.

The installation of arrays of instruments with common timing over an area of certain dimensions allows, for the first time, the possibility of reproducing the deformation of the Earth's surface caused by earthquake ground motions. To do so we produce a set of images (frames) showing the deformation of the entire array at each time step. For easier viewing, the recording stations in the array are interconnected by straight lines in an adequate order. The stations and lines move together giving an image of the motion of the array as waves are coming in. The superposition of relative locations of the entire array for a few time steps gives details of certain wave phases whereas an animation of many individual frames produces the representation of wave propagation.

The advantage of array displays over individual station displays is that the array images produced permit one, at a single glance, to obtain qualitative information and trends in the motion not just between different stations but also between 2 or 3 components of ground motion.

---

[1](CSO) Laboratorio Nacional de Engenharia Civil, Av Brasil, 1799 Lisboa Codex

[2](AJHL) Seismographic Stations, University of California, Berkeley, California 94720

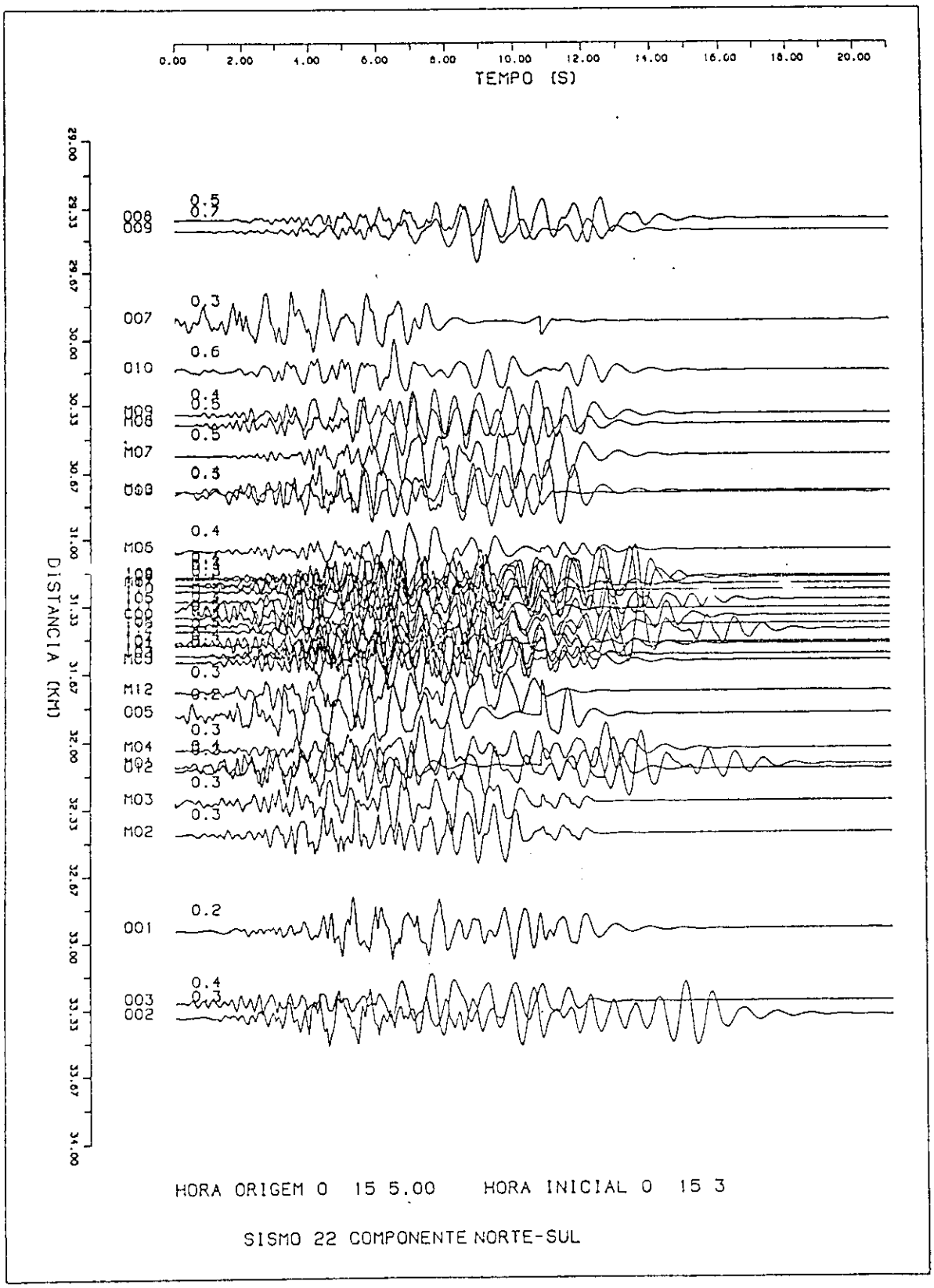

Figure 3. Record-section of event #22 along the epicentral direction

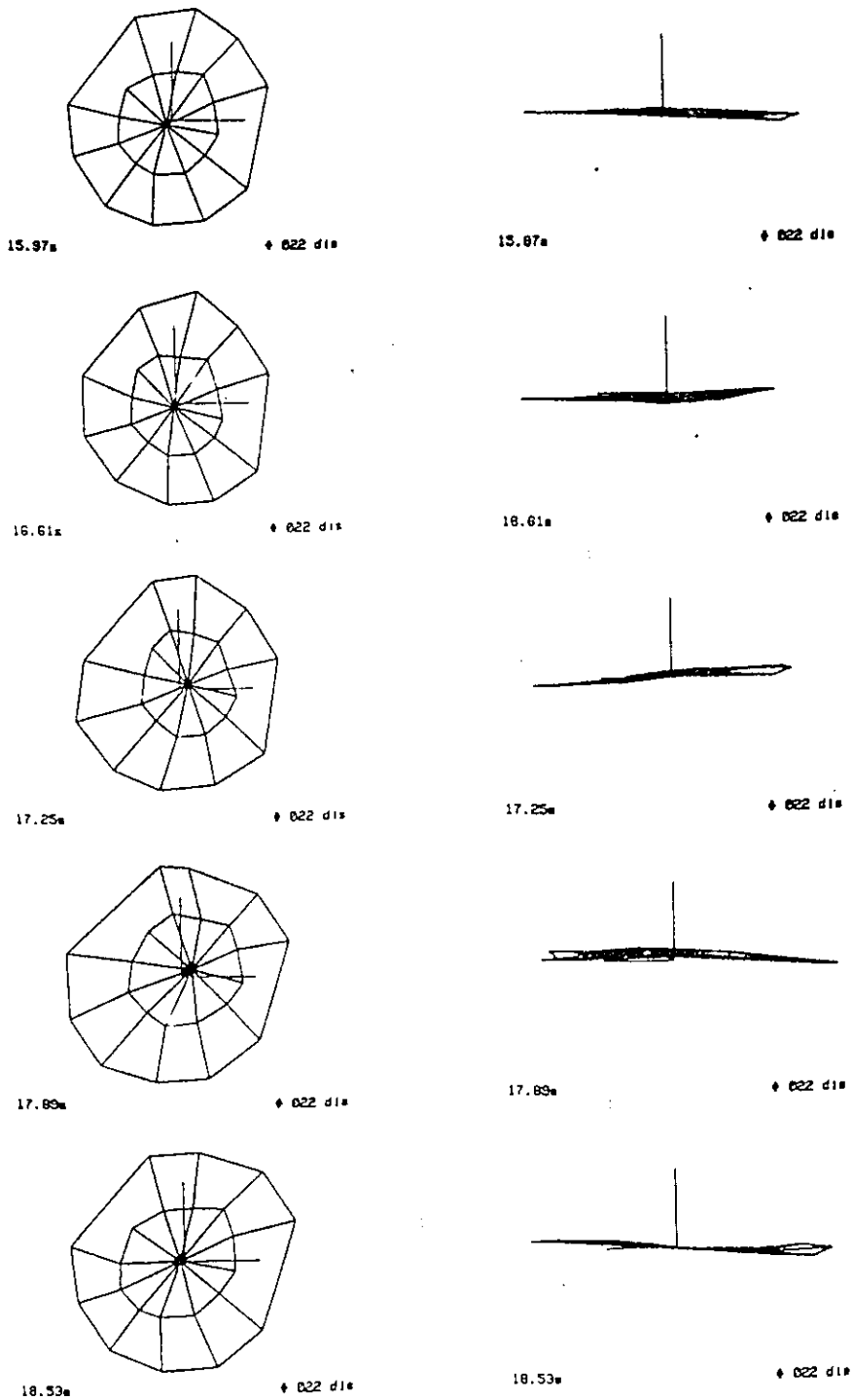

Figure 5. Individual frame images of displacement traces for event #22: time intervals Δt=0.64 sec during 6.40 sec; views from "over" the array (elevation of 11,500m) and from the plane of the array - "azimuthal" (distance from the center station of 9500m and azimuth of 45°); exaggeration 25,000 times for the "over" view and 50,000 times for the "azimuthal" view. Only M+O stations are represented. (The two straight lines at 90° show the initial array position at the C-00 station)

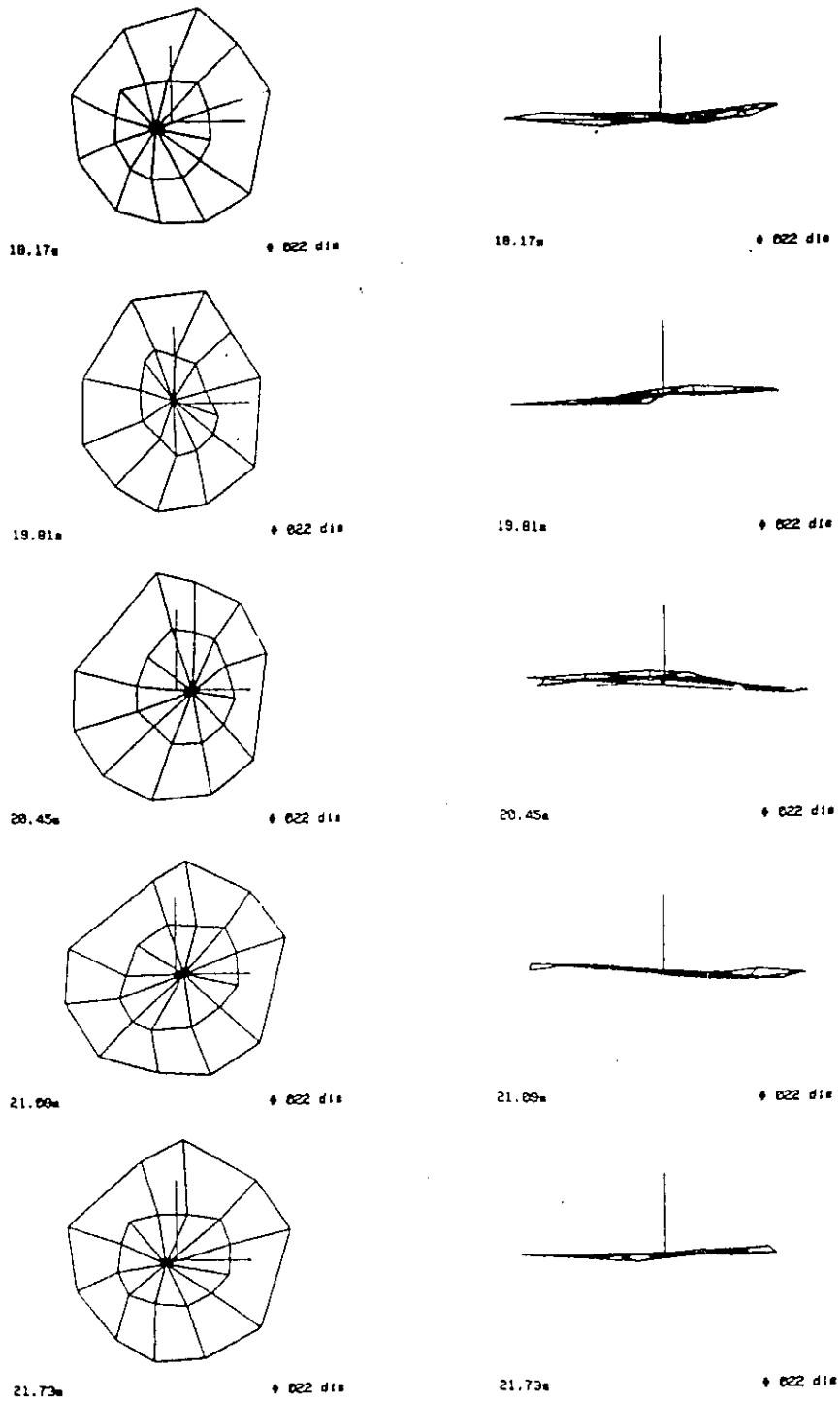

Figure 5. Continuation